



Low-dimensional analysis and modelling of the flow over a forward-facing step

B. Podvin^{1,†} and Y. Fraigneau²

¹EM2C, Centralesupélec, CNRS, Université Paris-Saclay, 91190 Gif/Yvette, France

²LISN, CNRS, Université Paris-Saclay, 91405 Orsay, France

(Received 2 August 2024; revised 13 October 2024; accepted 30 October 2024)

We consider the direct numerical simulation of the flow over a forward-facing step protruding in a turbulent boundary layer. Proper orthogonal decomposition (POD) is applied to the velocity field in different regions using Fourier modes in the spanwise direction. The upstream flow is characterized by a structure with a spanwise modulation of the order of the step height, the origin of which is consistent with a centrifugal instability. The structure is associated with ejections over the step of low-speed fluid from the upstream recirculation, and organized into streaks through the action of strong spanwise motions along the step face. The spanwise-averaged instantaneous momentum deficit created by the ejections is directly related to the maximal shear rate at the edge of the step, and is well correlated with the dynamics of the downstream recirculation. The most energetic patterns consist of three-dimensional motions with a large spanwise wavelength located in the shear layer developing at the edge of the step, as well as two-dimensional fluctuations downstream of the reattachment. A linear model based on the interaction of the mean flow with the dominant POD modes is able to recover the main frequencies of the fluctuations at these wavenumbers. Including the time variations of the ejections into the model yields temporal spectra that resemble qualitatively those computed from the simulation. The results suggest that the global dynamics of the flow are at least partly driven by linear mechanisms and depend on the characteristic structure identified in the upstream region close to the step.

Key words: low-dimensional models, boundary layer separation

1. Introduction

The flow over a step is of interest for a number of engineering applications, such as wind turbines, heat exchangers, combustion chambers, as well as transport vehicles. Its behaviour is dictated by the physics of separation, as it is characterized by two recirculation

† Email address for correspondence: berengere.podvin@centralesupelec.fr

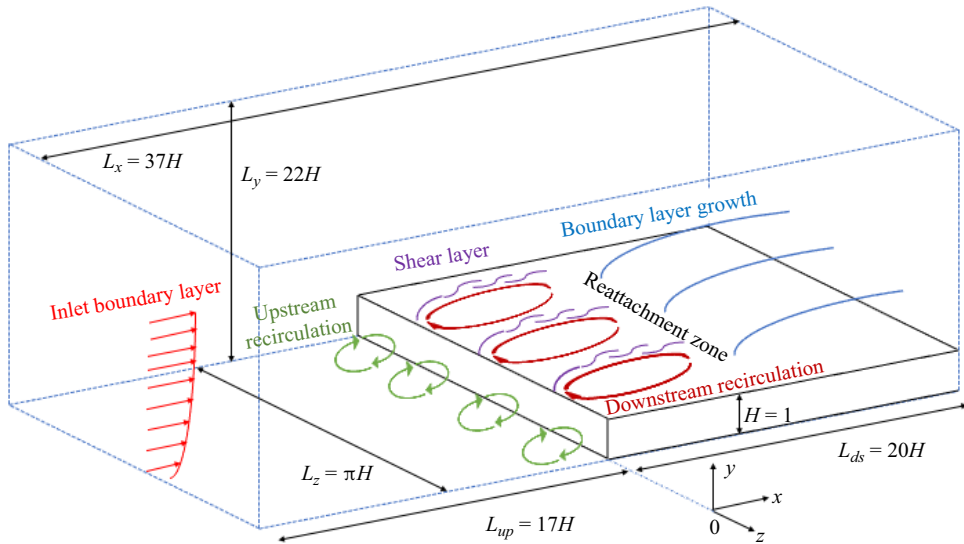


Figure 1. Numerical configuration (not to scale).

zones or bubbles, one at the base of the step and one on top of the step (as illustrated in figure 1). The dynamics of separated flows involve a wide range of frequencies, which are generally divided into three ranges: low frequencies, generally associated with ‘flapping’ or ‘breathing’ of the recirculation; medium frequencies, associated with large-scale vortex shedding downstream of the recirculation; and high frequencies, associated with instabilities in the developing shear layer and small-scale turbulence (Kiya & Sasaki 1983; Weiss, Mohammed-Taifour & Schwaab 2015; Tenaud *et al.* 2016).

Although the flow can be assumed to be statistically two dimensional if the width-to-height ratio of the step is large enough ($W/H > 6-10$ Martinuzzi & Tropea 1993; Sherry, Jacono & Sheridan 2010), its fluctuations are inherently three dimensional (Largeau & Moriniere 2007). Hammond & Redekopp (1998) showed that globally unstable dynamics can be expected in a recirculation bubble if the backflow velocity reaches 30 % of the incoming velocity. Lanzerstorfer & Kuhlmann (2012) carried out linear stability analysis of channel flows with various constriction ratios and identified a three-dimensional (3-D) global critical mode in the recirculation zone on top of the step, consisting of stationary streaks with a wavelength equal to three times the step height. The sensitivity of the flow to upstream conditions has been documented in experimental studies (Stuer, Gyr & Kinzelbach 1999), as well as in numerical studies (Wilhelm, Hartel & Kleiser 2003; Marino & Luchini 2009; Lanzerstorfer & Kuhlmann 2012). A major finding of these studies is that convective instabilities developing upstream can influence the formation of instabilities at the step face.

The upstream region of the step has therefore been the focus of specific investigation (Pearson, Goulart & Ganapathisubramani 2013; Graziani *et al.* 2018). The existence of streaky structures fed by spanwise motions along the step face was supported by the experimental observations of Martinuzzi & Tropea (1993), Stuer *et al.* (1999), Largeau & Moriniere (2007) and Pearson *et al.* (2013). In the case of an immersed step, where the step height H is smaller than the boundary layer thickness δ ($\delta/H = 1.47$), Pearson *et al.* (2013) were able to relate ejections over the step with the convection of low-velocity regions originating in the upstream boundary layer, thereby establishing a connection

between the upstream and downstream region. Graziani *et al.* (2018) examined the case of a protruding step ($\delta/H = 0.49$) and found evidence that the downstream recirculation was at least partly driven by the low-frequency oscillations of the upstream recirculation, in that the enlargement of the upstream separation was associated with a contraction of the downstream separation. Evidence of an anti-correlation was also found by Fang *et al.* (2021) in the case of an immersed step ($\delta/H = 2$), while a previous study by the same group (Fang & Tachie 2020) found a positive correlation when the step was placed in a rough turbulent boundary layer such that $\delta/H = 6.5$.

These results confirm that the spatio-temporal characteristics of the recirculation zones depend on various parameters of the incoming boundary layer, such as the ratio δ/H , the turbulence level and the Reynolds number based on the external velocity U and the boundary layer thickness δ . A discussion of the influence of these parameters can be found in Sherry *et al.* (2010). When the step is immersed in the boundary layer ($\delta/H > 1$) (Pearson *et al.* 2013; Fang *et al.* 2021), the flow on top of the step is then subject to strong mixing, which tends to reduce the size of the separation zone, but is also dependent on the velocity gradients and, therefore, the Reynolds number. As δ/H increases, the size of the downstream recirculation decreases (Largeau & Moriniere 2007). Moss & Baker (1980), Kiya & Sasaki (1985) have shown that a higher turbulence intensity results in a higher growth rate of the roll-up vortices developing in the shear layer between the separation point and the reattachment zone. The higher entrainment rate associated with larger vortices leads to a reduction of the separation zone. Sherry *et al.* (2010) showed that for several different ratios δ/H , two regimes could be identified, with a cutoff value of $Re_h = 8500$ that appears to be independent of δ/H : a low-Reynolds-number regime, where the recirculation length increases linearly with the Reynolds number, and a high-Reynolds-number regime, where it seems to be essentially independent from the Reynolds number, and which Sherry *et al.* (2010) attribute to the shear layer becoming turbulent at separation. In addition, the influence of the wall on the development of the shear layer is still an open question. McGuiness (1978) studied the internal separated flow at the inlet to a parallel pipe and found that the shear layer development was very similar to that of a mixing layer without the presence of the wall over most of the recirculation length, while wall effects operated close to reattachment.

Different statistical tools have been used to understand the physics of the flow over the step, including cross-correlations (Largeau & Moriniere 2007), as well as quadrant analysis of the turbulent motion (Hattori & Nagano 2010). Proper orthogonal decomposition (POD), a statistical technique (Lumley 1967) that extracts characteristic patterns from turbulent flows in an energetically optimal manner, has been applied to experimental measurements (Pearson *et al.* 2013; Graziani *et al.* 2018; Fang & Tachie 2020) as well as numerical data (Fang & Tachie 2020; Fang *et al.* 2021). As far as we know, in experimental as well as numerical studies, POD has been only limited to plane sections in the case of the forward-facing step, despite the 3-D nature of the flow. However, application of POD to volumes has been shown to be well suited for the analysis and low-order model reduction of complex turbulent flows (see, for instance, Aubry *et al.* 1988; Podvin *et al.* 2021).

In the present paper, a fully 3-D POD analysis of the flow is carried out for the flow over a step protruding from a turbulent boundary layer $\delta/H < 1$. Owing to spatial homogeneity of the geometry, POD modes in the spanwise direction are by construction Fourier modes, so that the decomposition is applied independently for each Fourier spanwise mode. In this framework, the approach is to construct a low-dimensional representation for the flow in order to better understand its underlying physics and to model its dynamics. The first step is

therefore to identify the features of the most energetic patterns upstream and downstream of the step, which constitute the building blocks of the representation. The next step is to use this representation to investigate the connection between the upstream and the downstream regions. The goal is then to construct a reduced-order model that can capture the main flow dynamics. The paper is therefore organized as follows. After a description of the numerical set-up in § 2, we present a brief review of POD in § 3. The flow in the upstream region of the step is discussed in § 4. Section 5 provides a description of the dominant dynamics over the step. The connection between the two recirculation zones is examined in § 6. A model to predict the amplitudes of the most energetic fluctuations is presented in § 7. A conclusion is given in § 8.

2. Configuration

2.1. Set-up

The configuration, shown in figure 1, consists of a two-dimensional (2-D) forward-facing step of height H , which will be the reference length throughout the paper. The Reynolds number Re based on the incoming velocity U and step height is 8300. The streamwise, vertical and spanwise directions will be respectively referred to as x , y , z and the velocity components as u , v , w or, equivalently, u_1 , u_2 , u_3 . The bottom end of the domain consists of an impermeable wall. A symmetry condition is imposed at the top end. No corrections for blockage effects are applied. Periodic boundary conditions are used in the spanwise direction.

The dimensions of the domain are $(L_x, L_y, L_z) = [37, 22, \pi]H$. The step is located at the origin of the domain at a distance of $17H$ from the upstream end. A convective boundary condition is used at the outlet of the domain with a correction procedure to ensure the mass flow rate conservation. The domain length is long enough to prevent small perturbations generated by the outlet conditions from spreading into the region of interest for the study. Turbulent inlet boundary conditions were implemented using the synthetic eddy method of Pamies *et al.* (2009) and the mean velocity profile was given by the numerical data of Spalart (1988) (AGARD database) for a turbulent boundary layer with a zero pressure gradient at a Reynolds number based on the momentum thickness $Re_\theta = 300$. Validation of the synthetic procedure was carried out for a turbulent boundary layer in the absence of a step. It also made it possible to define the boundary layer thickness to step height ratio δ/H , where δ was estimated as the flat plate boundary layer thickness at the same streamwise position as the step. It was found that $\delta/H \sim 0.8$, which means that the step is slightly protruding from the boundary layer. In all that follows, unless specified otherwise, all quantities will be expressed in terms of the step height H and incoming velocity U .

2.2. Numerical method and implementation

The incompressible Navier–Stokes equations were solved with the in-house code SUNFLUIDH (Fraigneau 2024), which is based on a second-order finite volume formulation. The spatial discretisation of convective and viscous terms is carried out with a second-order centred scheme on a staggered Cartesian grid following a MAC approach (Harlow & Welch 1965). A second-order backward formulation is used for the time derivative, with a semi-implicit treatment of the viscous term in order to strengthen the numerical stability in regard to the time step. An incremental projection method is used to compute the pressure field (Goda 1979; Guermond, Mineev & Shen 2006). For each time step, a predicted velocity field is obtained from integration of the Navier–Stokes equations by means of the alternating-direction implicit method (Peaceman & Rachford 1955;

	Δx_{min}	Δx_{max}	Δy_{min}	Δy_{max}	Δz
Upstream region (boundary layer) ($x < -H$; $0 < y < H$)	12.2+	12.2+	0.30+	4.05+	3.68+
Upstream region (footstep bubble) ($-H < x < 0$; $0 < y < H$)	4.5+	4.5+	0.30+	4.05+	3.68+
Downstream region (over-step bubble) ($0 < x < 4H$; $H < y < 2H$)	4.5+	4.5+	0.34+	4.05+	3.68+
Downstream region (boundary layer) ($4H < x$; $H < y < 2H$)	4.5+	10.8+	0.34+	4.05+	3.68+

Table 1. Spatial resolution of the computational grid in wall units.

Beam & Warming 1976). The pressure field is then computed by solving Poisson’s equation with a relaxed successive over-relaxation method coupled with a geometric multigrid method to improve the convergence of the solution. The solution of Poisson’s equation allows us to update both the pressure field and the velocity field so that the latter has a divergence-free property. A complete description of the algorithm is presented in Faugaret *et al.* (2022). This code has already been used for a number of studies, including bluff-body flows (Podvin *et al.* 2021).

The domain was divided into 200 subdomains ($5 \times 4 \times 4$ upstream of the step and $10 \times 3 \times 4$ downstream of the step), each of which had a grid size ($128 \times 192 \times 96$). The cell sizes ranged from 0.01 to 0.027 in the streamwise direction x , 0.00013 to 0.075 in the wall-normal direction in order to better resolve the flow near the surfaces, near the step edge and the shear layer growth capping the recirculation bubble downstream of the step. The spanwise resolution was uniform and equal to 0.0082. Table 1 sums up the spatial resolution of the grid in the main regions of interest. The resolution is expressed in wall units based on conditions at the inlet ($Re_\theta = 300$). The time step was constant and taken equal to 4.510^{-4} units, which yielded a Courant–Friedrichs–Lewy value of less than 0.4 over the range of integration. The simulation was run for 730 time units, which required about 900 000 CPU hours on the HPE SGI 8600 cluster at IDRIS (Institut du Développement et des Ressources en Informatique Scientifique). Data acquisition of 3-D flow fields was carried out once statistical convergence was established. The DNS results used in this study are part of the database <https://datasetmeca.lisn.upsaclay.fr/>.

2.3. Flow statistics

Sufficiently far away from the step, the flow corresponds to that of a flat plate boundary layer. A good agreement of the profiles with recent experimental results has been established in Larose *et al.* (2024). The mean velocity profile and turbulent intensities at $x = -6.6$ are represented in figure 2 and agree well with the results of Spalart (1988). The shape factor, defined as the ratio between the displacement and the momentum thicknesses δ_1/θ , is higher by 6 % (1.64 for a Reynolds number based on the momentum thickness of $Re_\theta = 570$) than in the flat plate case (1.55, Erm & Joubert 1991), which suggests that the influence of the step begins to be felt at this distance.

The streamwise component of the time-averaged velocity $U = \langle u \rangle$, where $\langle \cdot \rangle$ represents a time average, is shown in figure 3(a). The flow experiences an adverse pressure gradient as it approaches the step. Two recirculation zones, one upstream and one downstream, are delimited by a black line corresponding to the contour $U = 0$. The centre of the upstream recirculation zone is located at $x = -0.4$, with a separation point located at $x = -1.6$ and extends up to $y = 0.55$. The recirculation length of the downstream zone is about $x_R = 4.3$, which is in good agreement with results from the literature (Moss & Baker 1980; Largeau & Morinier 2007). The height of the downstream recirculation is about 0.25.

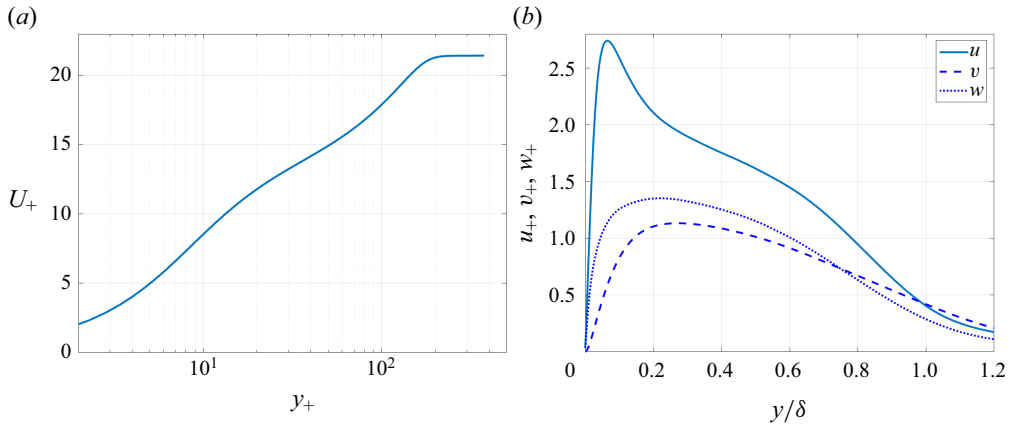


Figure 2. Mean velocity field and turbulent intensities $u^{i,rms}$ at $x = -6.6$. Wall units are based on the wall shear at $x = -6.6$.

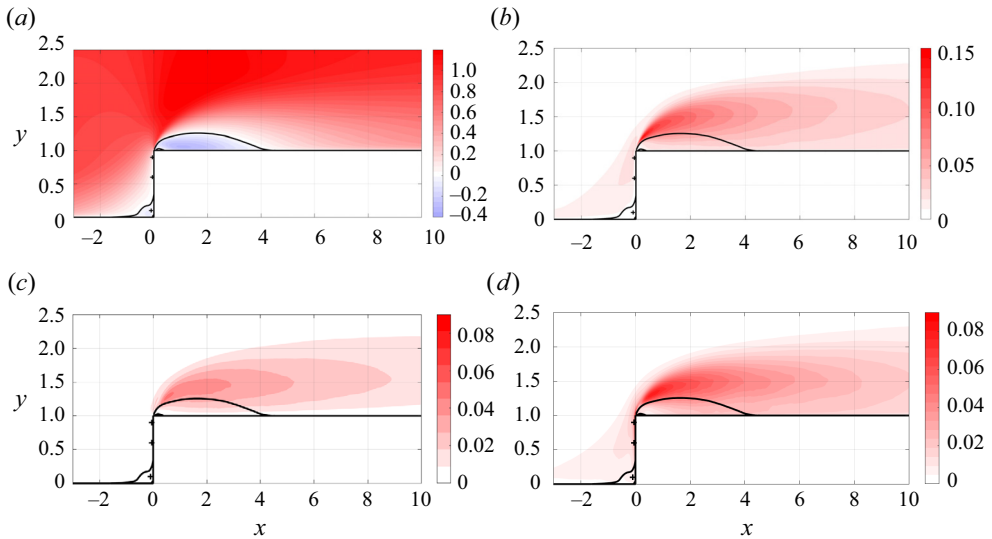


Figure 3. (a) Mean streamwise profile $\langle U \rangle$, (b) streamwise variance u^2 , (c) vertical variance v^2 and spanwise variance w^2 . The crosses correspond to the positions of the origin of the streamlines in figure 10. The averages were taken in time and in the spanwise direction. Results are shown for (a) $\langle U \rangle$, (b) $\langle u^2 \rangle$, (c) $\langle v^2 \rangle$ and (d) $\langle w^2 \rangle$.

The variance of each component of the fluctuations is shown in figure 3(c,d). The fluctuations are maximal in the shear layer developing at the edge of the step above the separation bubble. The streamwise component is dominant and the spanwise fluctuations are more intense than the wall-normal fluctuations.

The pressure coefficient on the step is shown in figure 4. Comparison with data from Farabee & Casarella (1986) and Hahn (2008) corresponding to slightly immersed cases $\delta/H = 2.4$ and $\delta/H = 1.5$ shows a very good agreement upstream of the step, with similar maximum values in the downstream area. We observe however a variation in the size of the adverse pressure gradient region downstream of the step, which could be due to the difference between the experimental (immersed) set-ups and our numerical (slightly

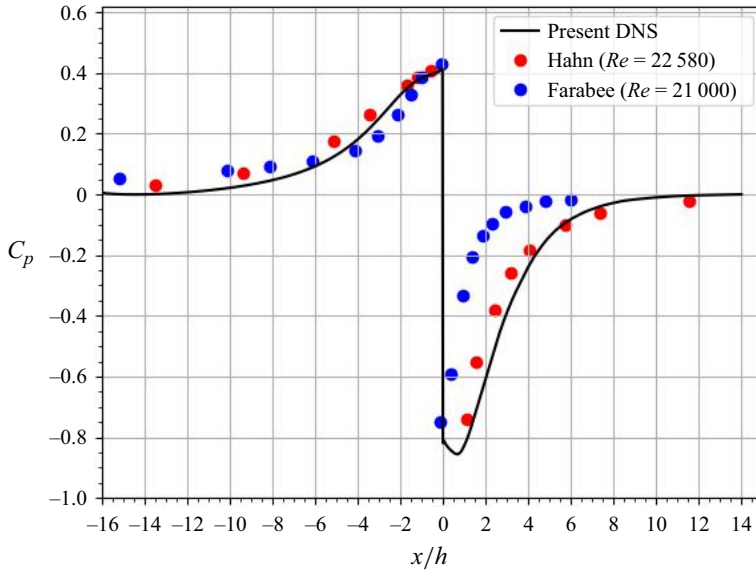


Figure 4. Mean pressure coefficient over the step. Comparison with the experimental data of Hahn (2008) and Farabee & Casarella (1986). The averages were taken in time and in the spanwise direction.

protruding) configuration. We note that better agreement is obtained for the ratio of 1.5 (Hahn 2008) that is closer to our case.

3. Proper orthogonal decomposition

Our analysis of velocity fluctuations will be based on POD. Proper orthogonal decomposition is a statistical technique (Lumley 1967) that decomposes any spatio-temporal field \underline{q} defined over a domain Ω into a sum of spatial modes $\underline{\Phi}$, the amplitudes of which vary in time. The spatial modes $\underline{\Phi}$ are the principal directions of the autocorrelation tensor, which is built from a collection of fields or snapshots. The modes are optimal in the sense that the reconstruction error between the original snapshots and any linear reconstruction based on N modes is minimal for the POD modes.

Due to the statistical homogeneity in the spanwise direction (z), POD modes are Fourier modes in that direction (Holmes, Lumley & Berkooz 1996). The decomposition is therefore applied in Fourier space in the spanwise direction and any field \underline{q} can be written as

$$\underline{q}(x, y, z, t) = \sum_k \hat{q}_k e^{i2\pi kz/L_z} + \text{c.c.} = \sum_k \sum_n \sqrt{\lambda_k^n} a_k^n(t) \underline{\Phi}_k^n(x, y) e^{i2\pi kz/L_z} + \text{c.c.}, \quad (3.1)$$

where c.c. represents the complex conjugate. Here \underline{q} will be taken equal to the fluctuating velocity $\underline{q} = \underline{u} - \underline{U}$. The positive quantity $\sqrt{\lambda_k^n}$ represents the contribution of the mode $\underline{\Phi}_k^n$ to the variance of the fluctuations. The spatial modes $\underline{\Phi}_k^n$ and temporal amplitudes a_k^n are complex for $k \neq 0$ and purely real for $k = 0$. By construction, at each spanwise Fourier wavenumber, the spatial modes are orthogonal and the temporal amplitudes uncorrelated. They are also normalized so that $\int_{\Omega} \underline{\Phi}_k^n \cdot \underline{\Phi}_m^{m*} dx dy = \delta_{nm}$ and $\langle a_k^n a_k^{m*} \rangle = \delta_{nm}$, where $*$ represents the complex conjugate. For each spanwise wavenumber k , the amplitudes $a_k^n(t)$ and modes $\underline{\Phi}_k^n$ are obtained by applying the method of snapshots (Sirovich 1987) to the

temporal correlation matrix obtained from N_s snapshots, i.e.

$$C_k^{mp} = \frac{1}{N_s} \int_x \int_y \hat{q}_k(x, y, t_m) \hat{q}_k^*(x, y, t_p) dx dy, \quad (3.2)$$

and solving the eigenproblem

$$C_k^{mp} A_k^{pn} = \lambda_k^n A_k^{mn}, \quad (3.3)$$

where the n th column of the matrix A is such that $A_k^{pn} = a_k^n(t_p)$, and a summation convention is used for the p index. Here λ_k^n represents the contribution of the n th POD mode to the k th Fourier mode of the correlation. Since $\lambda_{-k}^n = \lambda_k^n$ for $k > 0$, only the positive part of the spectrum will be represented. However, to account for the contribution of both negative and positive wavenumbers to the variance, we used a rescaling factor of 2 when representing the eigenvalues at non-zero wavenumbers.

The modes $\underline{\Phi}_k^n(x, y)$ can be obtained from

$$\underline{\Phi}_k^n(x, y) = \frac{1}{\sqrt{\lambda_k^n}} \sum_{p=1}^{N_s} a_k^n(t_p) \hat{q}_k(x, y, t_p). \quad (3.4)$$

Equation (3.3) shows that each vector of amplitudes A_k^n and, therefore, each spatial mode $\underline{\Phi}_k^n(x, y)$ is defined within an arbitrary phase.

We denote $\phi_k^{n,i}$ the i th velocity component of the n th POD mode associated with the k th Fourier wavenumber. The number of snapshots was taken to be 940 fields, separated by 0.5 convective time units. No significant change in the dominant modes was observed when only 600 fields were considered. Since the fluctuations are dominant downstream of the step, POD was first limited to the upstream region close to the step in order to extract local energetic motions there. We then applied POD to the velocity in a volume comprising the upstream region and a region downstream of the step. The labels *up* and *ds* will be used to refer respectively to the upstream and the downstream region to remove possible ambiguity, but will be omitted otherwise.

4. Upstream dynamics

4.1. Dominant motions

A first description of the flow is given by the spatial distribution of the lowest and most energetic spanwise Fourier modes for each velocity component, which is represented in figure 5 for the region directly upstream of the step. The vertical velocity is most important for the lower wavenumbers $k = 1$ and $k = 2$ with a maximum at the step mid-height. The streamwise component is most important for modes $k = 3$ and $k = 4$ with a maximum close to the step corner at $x = -0.3$ and $y = 0.7$. It is also associated with strong spanwise components along the step face close to the edge.

Proper orthogonal decomposition was applied to the fluctuating velocity field in the upstream region $\Omega_x^{up} \times \Omega_y^{up} \times \Omega_z^{up} = [-6, 0] \times [0, 1.5] \times [0, \pi]$. The POD eigenvalues $\lambda_k^{n,up}$ are shown in figure 6 for the first spanwise wavenumbers. As expected from the energy spectra in figure 5, the largest eigenvalues $\lambda_k^{1,up}$ correspond to the wavenumbers $k = 2, 3, 4$, and are about equal. For these wavenumbers, the first eigenvalue λ_k^n is more than twice as large as the next one, which indicates the importance of 3-D coherent motions associated with the first mode. The eigenvalues λ^n decay as n^{-1} for higher-order modes.

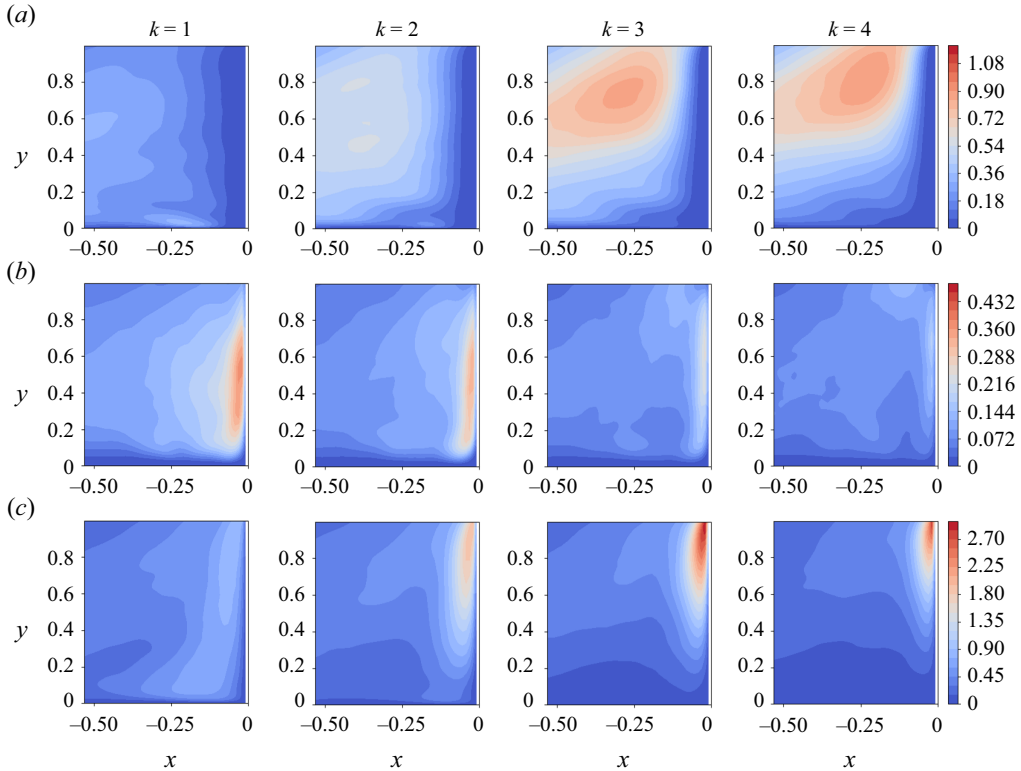


Figure 5. Spatial distribution of the spanwise Fourier transform of the velocity in the upstream region. (a) Streamwise component $\langle |\hat{u}_k|^2 \rangle$, (b) vertical component $\langle |\hat{v}_k|^2 \rangle$, (c) spanwise component $\langle |\hat{w}_k|^2 \rangle$.

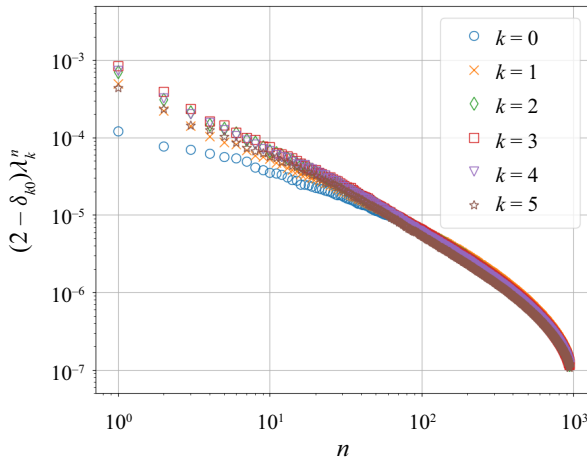


Figure 6. The POD spectrum $\lambda_k^{n,up}$ in the upstream domain. The eigenvalues are rescaled by the factor $2 - \delta_{k0}$ to account for the contribution of positive and negative wavenumbers.

The eigenvalue of the largest fluctuating spanwise invariant mode $\lambda_0^{1,up}$ is about an order of magnitude less than the dominant ones. The streamwise and the normal velocity components $\phi_0^{1,1(up)}$ and $\phi_0^{1,2(up)}$ are represented in figure 7 on which we also reported the streamline $\langle U \rangle = 0$ delimiting the recirculation zone. The step height is delimited with a

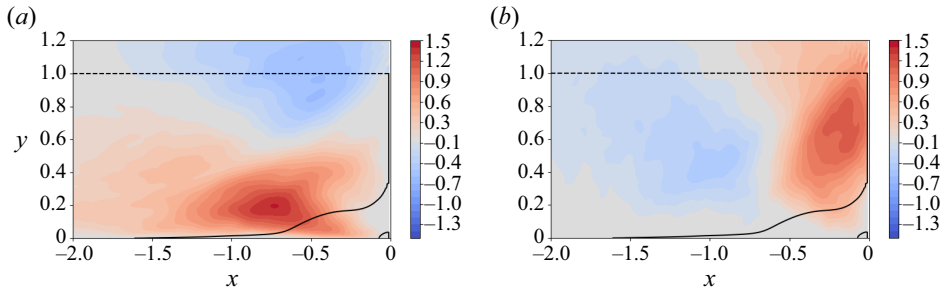


Figure 7. Velocity-based POD dominant spanwise invariant mode $\Phi_0^{1,up}$: streamwise (a) and vertical (b) component. The black line represents the $\langle U \rangle = 0$ contour. The dashed line represents the step height. Results are shown for (a) $\Phi_0^{1,1(up)}$ and (b) $\Phi_0^{1,2(up)}$.

horizontal dashed line. The mode is characterized by a strong horizontal motion close to the edge of the recirculation in the region $y < 0.5$, which coincides with a vertical motion of nearly equivalent intensity along the step face above the recirculation in the region $x > -0.5$. A weaker horizontal (respectively vertical) motion of the opposite sign is observed in the region $y > 0.5$ (respectively $x < -0.5$). The mode $\Phi_0^{1(up)}$ therefore represents momentum transfer from the streamwise to the wall-normal direction: it constitutes a spanwise invariant vortex that oscillates non-harmonically back and forth.

The most energetic mode corresponds to $k = 3$ or $\lambda_z \sim 1.03$ and is shown in figure 8. Other dominant wavenumbers $k = 2$ and $k = 4$ were found to have generally similar features. The main wavelength λ_z is in good agreement with Fang *et al.*'s (2021) results, who found a dominant wavelength of 1.32. The streamwise component of the mode $\Phi_3^{1(up)}$ captures 70 % of its energy and is of constant sign over a region connecting the upstream boundary layer with the recirculation over the step. The mode is characterized by much weaker vertical fluctuations (5 % of the energy), which are negatively correlated with the streamwise component over the step, so that the corresponding pattern is consistent with ejections of low-speed fluid. Although the spanwise motion represents only 25 % of the total mode energy, it is characterized by intense fluctuations (twice as large as in the streamwise direction) in a very thin layer, which is less than 0.1 thick and extends from the top of the recirculation to over the top of the step. A weaker fluctuation of the opposite sign is also noticeable upstream of the step. The presence of both positive and negative fluctuations could be consistent with vortical motion aligned with the vertical axis along the step face.

The spectra of the amplitudes $a_k^{1,up}$ are represented in figure 9. Since the amplitudes are complex for non-zero Fourier modes, their Fourier transform is generally not symmetric in frequency space $\hat{a}_k^n(-f) \neq \hat{a}_k^{*n}(f)$. The presence of a significant asymmetry in the spectrum can be associated with a persistent drift in physical space. In the present case the spectrum appears to be nearly symmetric, which does not make it possible to identify specific convective motions. The dominant part of the spectra for the different wavenumbers is located in the same low-frequency range $[0, 0.05]$, which suggests that their dynamics are connected.

4.2. Characteristic structure

The label *up* will be implicit throughout the paragraph. It would be helpful for physical interpretation to educe a characteristic spatial or coherent structure associated with the

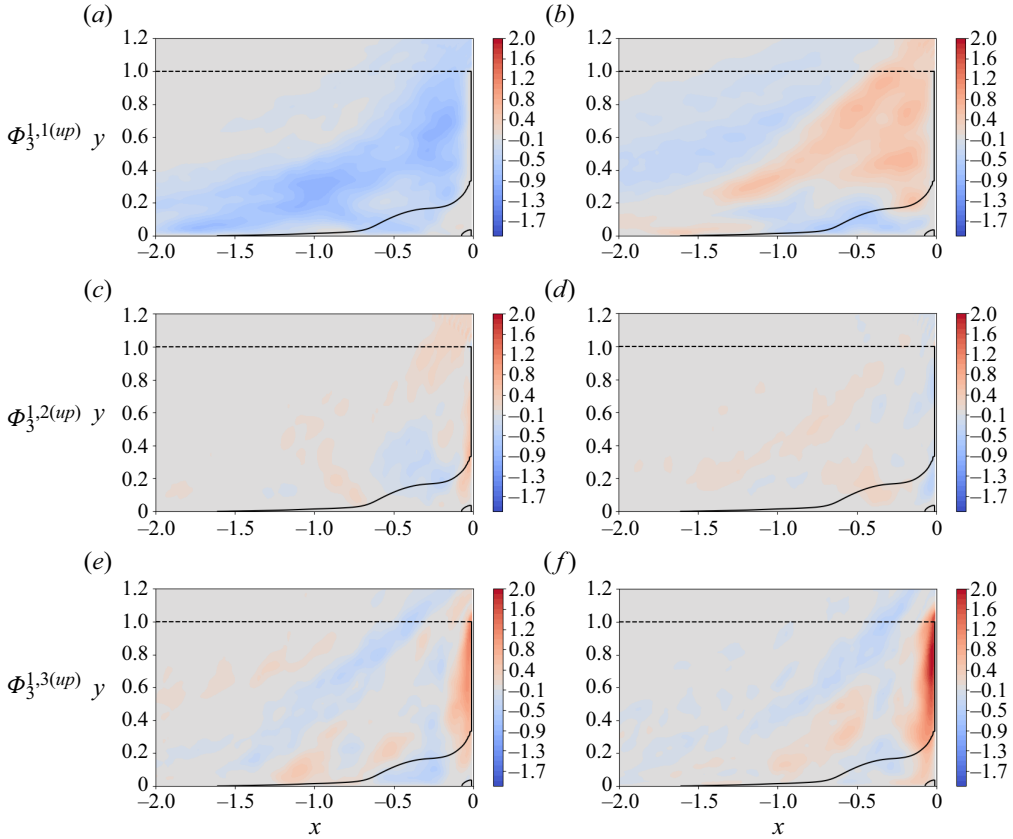


Figure 8. The POD velocity eigenmodes (a,c,e) $\text{Re}[\Phi_3^{1,up}]$ and (b,d,f) $\text{Im}[\Phi_3^{1,up}]$. From top to bottom row: streamwise, vertical and spanwise component. The black line represents the $\langle U \rangle = 0$ contour. The dashed line represents the step height.

dominant POD modes, that could be compared with experimental observations such as particle tracking velocimetry visualizations (Stuer 1999) or numerical approaches such as stochastic estimation (Fang *et al.* 2021). We note that reconstructing a physical structure from Fourier POD modes is different from applying POD directly in the physical space, since the temporal amplitude of each mode a_k^n also depends on the wavenumber. This means that each term $\sqrt{\lambda_k^n} a_k^n(t) \underline{\Phi}_k^n(x, y)$, which we rewrite as a product $a_k^n(t) \tilde{\underline{\Phi}}_k^n(x, y)$, where $\tilde{\underline{\Phi}}_k^n = \sqrt{\lambda_k^n} \underline{\Phi}_k^n$ corresponds to a convolution in physical space. As a result, the expansion

$$\underline{q}(x, y, z, t) = \sum_n \sum_k a_k^n(t) \tilde{\underline{\Phi}}_k^n(x, y) e^{i2\pi kz/L_z} = \sum_n \int_{z'=0}^{\pi} a^n(t, z') \underline{\Phi}^{n,C}(x, y, z - z') dz'. \tag{4.1}$$

If the average energy of the k th Fourier component of a^1 is taken to be 1, it follows that the k th Fourier component of $\underline{\Phi}^{1,C}$ is given by the POD mode $\lambda_k^1 |\underline{\Phi}_k^1(x, y)|^2$. However, this is not enough to reconstruct $\underline{\Phi}^{1,C}$ in physical space as the phases of the Fourier components are arbitrary. Additional assumptions are therefore required in order to determine $\underline{\Phi}^{n,C}$ in physical space. A discussion of this issue can be found in Holmes *et al.* (1996), who proposed a solution based on the determination of the bi-spectrum.

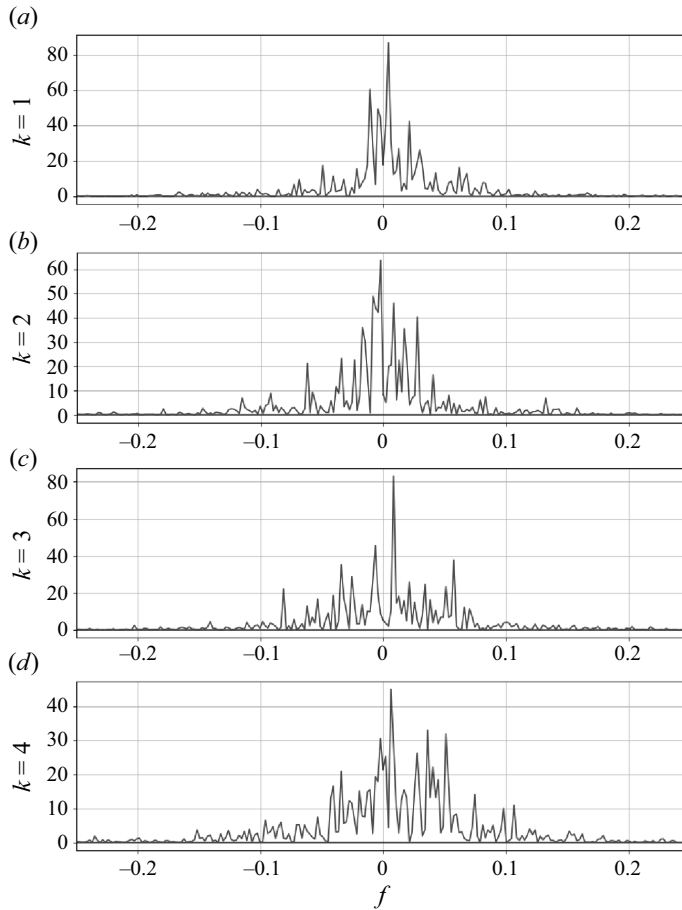


Figure 9. Temporal spectrum of the dominant upstream POD velocity amplitudes $|\hat{a}_k^{1,up}|^2$.

Moin & Moser (1989) applied this method to the case of a turbulent channel flow in order to educe a 'characteristic eddy' from 2-D Fourier mode components, but also explored alternative approaches based on eigenfunction continuity with respect to the wavenumber as well as spatial compactness.

Following their lead, we choose to guarantee spatial compactness of the structure, which is easy to do in one-dimensional Fourier space. As shown by Moin & Moser (1989), this means minimizing the phase difference between the modes – the Fourier coefficients should all be real and positive for the sum of the modes to reach its maximum. This will define a structure in physical space but will leave its absolute position in the spanwise direction arbitrary since due to homogeneity only the phase differences of the modes can be determined. We therefore computed for each mode $\underline{\Phi}_k^1$ an average phase α_k^1 over the domain and over each component, using

$$\alpha_k^1 = \sum_{i=1}^3 \iint_{\Omega_x^{up} \times \Omega_y^{up}} |\phi_k^{1,i}(x, y)|^2 |Arg[\phi_k^{1,i}(x, y)]| dx dy, \quad (4.2)$$

where $\phi_k^{1,i}$ is the i th component of the velocity POD mode and Arg is its argument. We recall that $\iint_{\Omega_x^{up} \times \Omega_y^{up}} \phi_k^{1,i}(x, y) \phi_k^{1,i*}(x, y) dx dy = 1$. A characteristic structure was then reconstructed from the dominant wavenumbers $k \leq 4$ as

$$\underline{\Phi}^{1,C}(x, y, z) = \sum_{k=-4}^4 \sqrt{\lambda_k^1} \underline{\Phi}_k^1(x, y) e^{2i\pi kz/L_z - \alpha_k^1}, \quad (4.3)$$

where the contribution $\underline{\Phi}_k^1$ of each wavenumber k to the sum was weighted by the characteristic intensity $\sqrt{\lambda_k^1}$. This determines the amplitude of the structure.

The streamlines of the field corresponding to the superposition of the mean flow and the reconstructed structure $\underline{\Phi}^{1,C}$ are represented in figure 10 for three different sets of original locations (both forward and backward time integration are performed). Each set of locations consists of a horizontal line along the step face: one close to the inward corner ($x = -0.05, y = 0.1$), one just above the mean recirculation ($x = -0.05, y = 0.6$) and one just above the step edge ($x = -0.05, y = 0.9$). Each type of streamline is associated with the same well-delimited spanwise regions of fluid upstream, illustrating the compactness of the representation. Visualization of the streaky pattern created by the structure is provided by representing the contour lines of the streamwise velocity in the vertical plane at the step corner $x = 0$ in each subplot. Different flow patterns associated with the characteristic structure $\underline{\Phi}^{1,C}$ can thus be identified.

Near the bottom wall (figure 10a), fluid from the incoming boundary layer gets trapped within the recirculation zone, but then leaves it after a few spins and is ejected over the step. A good agreement is found with experimental (Stuer *et al.* 1999) and numerical observations (Fang *et al.* 2021, figure 14a). The twisting and ejecting motions from within the recirculation zone are associated with open recirculation streamlines, which cannot be captured by a 2-D representation. Comparison of the incoming streamlines with the lifted-up streamwise velocity contours in the vertical plane at the step corner indicate that the ejected fluid is slower than the mean flow.

At mid-height (figure 10b), flow separation takes place, due to the strong spanwise motions close to the wall. Above the recirculation zone, the flow is collected into different low-speed streaks, which are then ejected over the step. Note that the location of these ejections generally coincides with the fluid leaving the recirculation. Just underneath the step at $y = 0.9$ (figure 10c), most of the flow streamlines spread out from upstream locations further away from the wall and are less likely to get trapped in the recirculation zone. As a result, they reach the wall with a higher velocity (as evidenced by the streamwise contour lines in the vertical plane) and without being shifted in the spanwise direction.

4.3. Centrifugal instability

We now investigate the origin of this structure. Due to the presence of the step, the mean flow is characterized by a strong curvature (see figure 3), so that a possible formation mechanism could be a centrifugal instability. A necessary condition for the existence of this instability is given by an inviscid criterion (Drazin & Reid 1982) based on the Rayleigh discriminant Ψ that, following Beaudoin *et al.*'s (2004) approach for a backward-facing step, can be defined as

$$\Psi = \frac{2U_m \Omega_z}{R}, \quad (4.4)$$

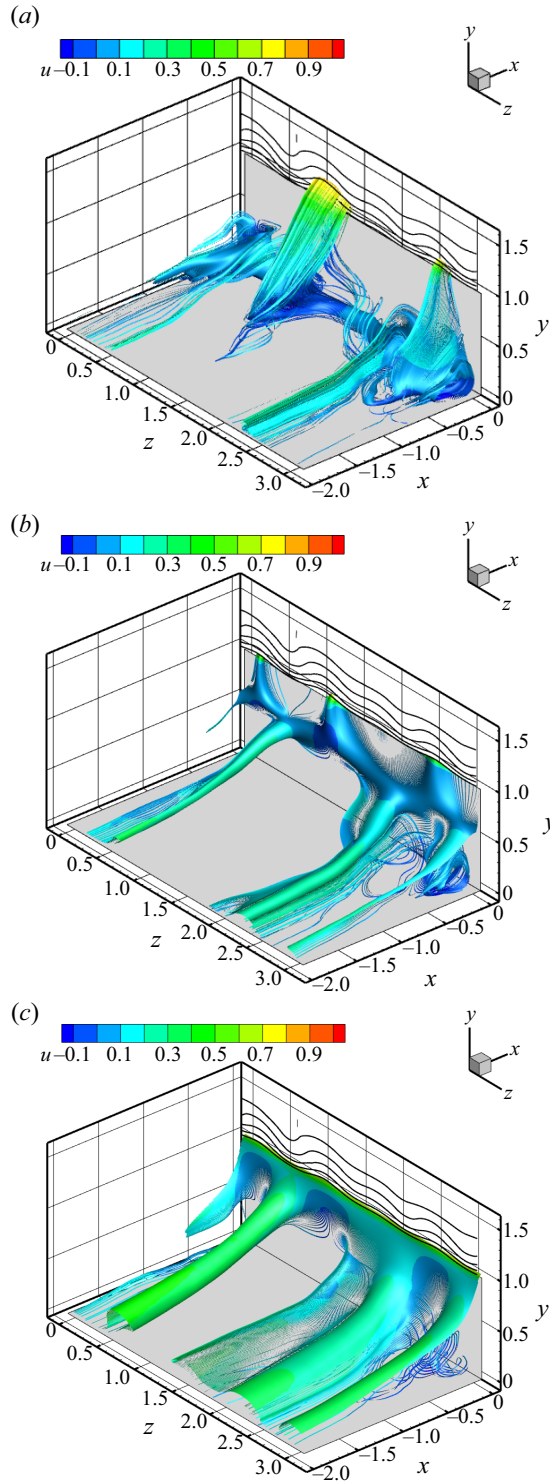


Figure 10. Streamlines of the characteristic upstream structure coloured by the streamwise velocity. Streamlines go through the lines $x = -0.1$, $y = 0.1$ (a); $x = -0.05$, $y = 0.6$ (b) and $x = -0.05$, $y = 0.95$ (c). See text for more details.

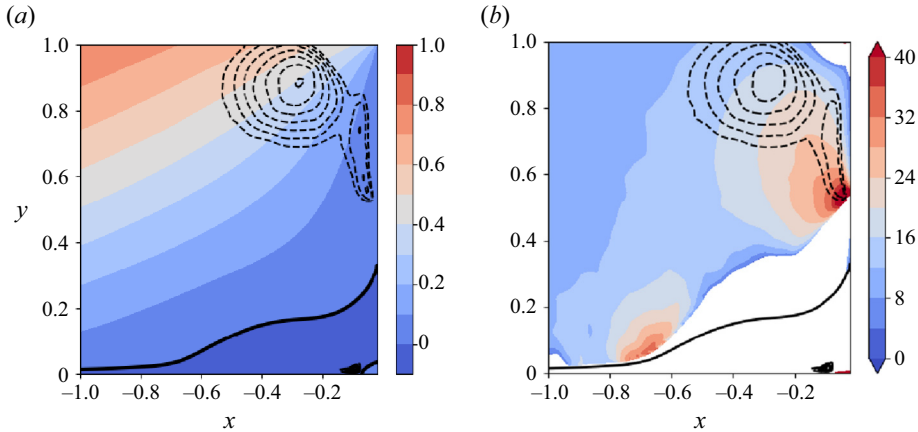


Figure 11. Contour lines of the Rayleigh discriminant Φ – values from -0.30 to -0.54 with increments of 0.03 . The lines are superposed with (a) the time-averaged streamwise velocity component U and (b) the local Görtler number (see text for definition). The region where the Rayleigh discriminant Φ is positive is coloured in white.

where $U_m^2 = U^2 + V^2$, $\Omega_z = \partial V / \partial x - \partial U / \partial y$ and R is the local radius of curvature obtained from Sipp & Jacquin (2000) as

$$R = \frac{(U^2 + V^2)^{3/2}}{Ua_y - Va_x}, \quad (4.5)$$

where a_x and a_y correspond to the components of the convective acceleration $\underline{U} \cdot \nabla \underline{U}$. When the Rayleigh discriminant is negative, the flow is potentially unstable to a centrifugal instability. The region where the Rayleigh discriminant is negative with a large modulus is represented in figure 11. It is characterized by two local minima corresponding to the respective local maxima of the streamwise and spanwise velocity fluctuations (see figure 5).

However, for instability to occur, curvature effects need to overcome the effect of viscosity, a relative measure of which is given by the Görtler number

$$Go = \frac{U_{fs} \delta^{3/2}}{\nu} R^{-1/2}, \quad (4.6)$$

where in the classical laminar Görtler problem (Saric 1994), δ corresponds to the boundary layer thickness and U_{fs} is the free-stream velocity (here $U_{fs} = 1$). Note that although we used a description based on a Görtler number, we did not find any clear evidence of Görtler vortices in the flow. In the present case, the flow is (weakly) turbulent and, as proposed by Tani (1962), the stability characteristics can be determined in a turbulent case if the viscosity is replaced by the turbulent eddy viscosity ν_t , for which we can use Clauser's law $\nu_t \sim 0.018U\delta_1$. Following Dagaut *et al.* (2021), we computed a turbulent Görtler number

$$Go = \frac{U_{fs} \delta_1^{3/2}}{\nu_t} R^{-1/2} = \frac{\delta_1^{1/2}}{0.018R^{1/2}}, \quad (4.7)$$

where the displacement thickness δ_1 was estimated at the position of the step in the flat plate turbulent boundary layer.

Figure 11 shows that the upper region close to the step edge is characterized by both a high Görtler number and strongly negative values of the Rayleigh discriminant.

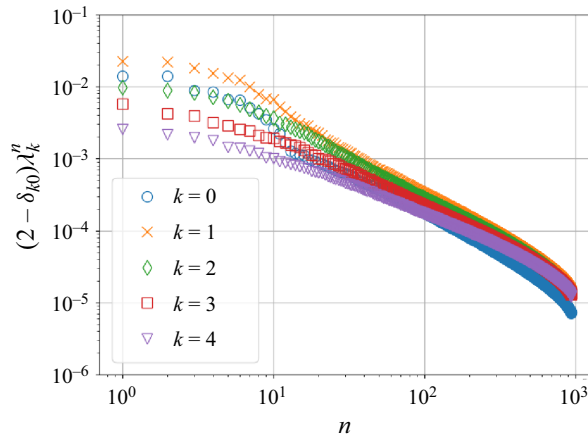


Figure 12. The POD spectrum λ_k^n in the full domain for the largest spanwise wavenumbers $k \in \{0, \dots, 4\}$. The eigenvalues are rescaled by the factor $2 - \delta_{k0}$ to account for the contribution of positive and negative wavenumbers.

Comparison of figure 11 with figure 5 suggests that the region around $x = -0.2, y = 0.8$, corresponding to the maximum streamwise fluctuation intensity, could be a good candidate for the origin of the instability. An interesting parallel can be drawn with Brès & Colonius’s (2008) study of the flow over a cavity. Using 3-D linear stability analysis and direct numerical simulation (DNS), they provided evidence of a centrifugal instability mechanism with a spanwise wavelength of the order of the cavity depth for shallow cavities, which is comparable with the dominant wavelengths found upstream of the step.

5. Full domain

Proper orthogonal decomposition was then applied to the domain consisting of both the upstream domain $\Omega_x^{up} \times \Omega_y^{up} \times \Omega_z^{up} = [-6, 0] \times [0, 1.5] \times [0, \pi]$ and the downstream region $\Omega_x^{ds} \times \Omega_y^{ds} \times \Omega_z^{ds} = [0, 7] \times [1, 7] \times [0, \pi]$. Figure 12 represents the dominant POD eigenvalues λ_k^n for the velocity for the first spanwise wavenumbers. As mentioned in § 3, the contribution of the negative wavenumbers was lumped with that of the positive ones, so that a factor α_k of 2 was used in the representation of the non-zero spanwise wavenumbers. Unlike the upstream case, the most energetic wavenumbers correspond to the lowest ones, i.e. $k = 0$ and $k = 1$, and several eigenmodes make nearly equally important contributions to the energy at each spanwise wavenumber, which indicates a relatively complex organization of the flow. The discussion in this section will be focused on the wavenumbers $k = 0$ and $k = 1$.

5.1. Zero spanwise modes

Figure 12 shows that the fluctuating velocity eigenvalues for the spanwise invariant modes $k = 0$ are organized in pairs, of the form $2n - 1, 2n$ for $n \geq 1$, particularly for the first three couples of modes. The corresponding velocity eigenmodes are represented in figure 13. One can see that they correspond to 2-D, roll-like structures shed from the downstream recirculation bubble. The streamwise component of the modes is important at the location of reattachment, which suggests that the modes could also be associated with the breathing or flapping motion of the separation bubble.

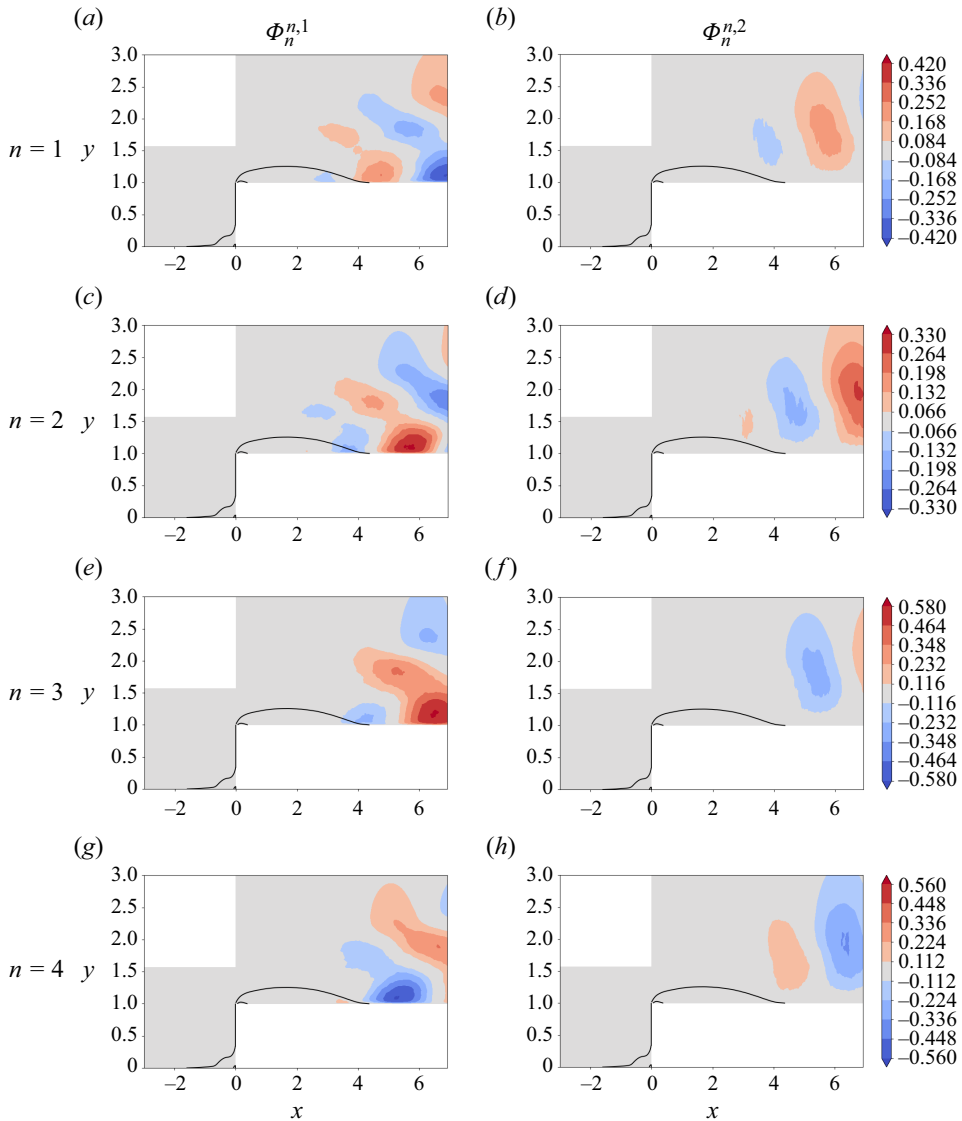


Figure 13. The POD eigenmodes Φ_0^n ; (a,c,e,g) streamwise component $\Phi_0^{n,1}$ and (b,d,f,h) vertical component $\Phi_0^{n,2}$. The black line represents the contour $\langle U \rangle = 0$.

The spectra of the corresponding amplitudes are represented in figure 14. One can see that the range of frequencies covered by the spanwise-averaged velocity is the same for each pair n . As we will see below, the organization of the modes into pairs is consistent with convective motion. For the first pair of eigenmodes, two frequencies, one around 0.10 and one around 0.13, can be identified. These values are consistent with the characteristic value of $f x_R / U = 0.6$ associated with vortex shedding (Kiyama & Sasaki 1983) since we have $x_R = 4.3$. For the higher-order pairs, the frequency at 0.10 can still be identified, but the dominant lower-frequency part of the spectrum is characterized by low frequencies while the high-frequency part shifts towards higher frequencies. A peak is observed around 0.03

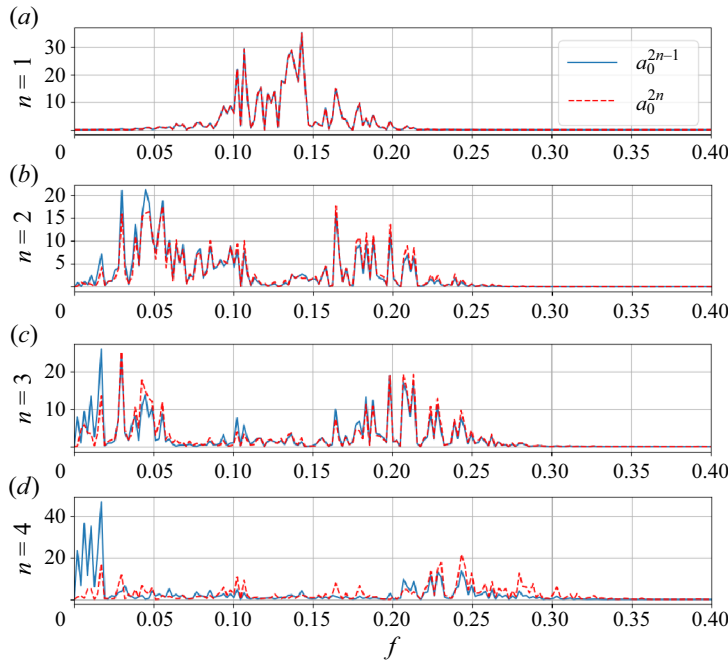


Figure 14. Temporal spectrum of the dominant POD velocity amplitudes $|\hat{a}_0^p|^2$, $p \in \{1, \dots, 8\}$.

in the low-frequency range, which is in good agreement with the non-dimensional flapping frequency of $f_{XR}/U = 0.12$ identified by Kiya & Sasaki (1983).

5.2. Dominant spanwise modes

The dominant wavenumber $k = 1$ corresponding to a wavelength λ_z of π is in good agreement with the critical mode of 3 identified by Lanzerstorfer & Kuhlmann (2012) and Wilhelm *et al.* (2003). The first six modes corresponding to this wavenumber are represented in figure 15. The spatial features of the modes are markedly different from those of the 2-D (spanwise invariant) modes: the signature of the shear layer extending above the separation bubble is clear, the modes extend within the recirculation zone and are characterized by a strong spanwise component, which is larger than the vertical component. The modes have different spatial scales: the first three modes are relatively large scale, while modes 4 and 5 are characterized by smaller scales, and mode 6 is characterized by a mixture of large and small scales.

Figure 16 represents the temporal spectrum of the corresponding amplitudes a_1^p . Unlike the upstream region, the modes are characterized by a strong dissymmetry, which is consistent with convective motion, as will be seen in more detail below. The first two modes are characterized by frequencies in the range 0.05–0.15 (in absolute value) with a peak slightly below 0.1, which is also observed for mode 3. However, mode 3 also contains energy in the range [0.1, 0.25], which is also important for mode 4. Mode 5 is characterized by a narrow range of frequencies around 0.22, while mode 6 contains a wide range of frequencies in the range [0.05, 0.3] with a low-frequency peak at 0.05. The overlap in frequency space supports the idea that the modes are physically connected to each other.

Low-dimensional analysis and modelling

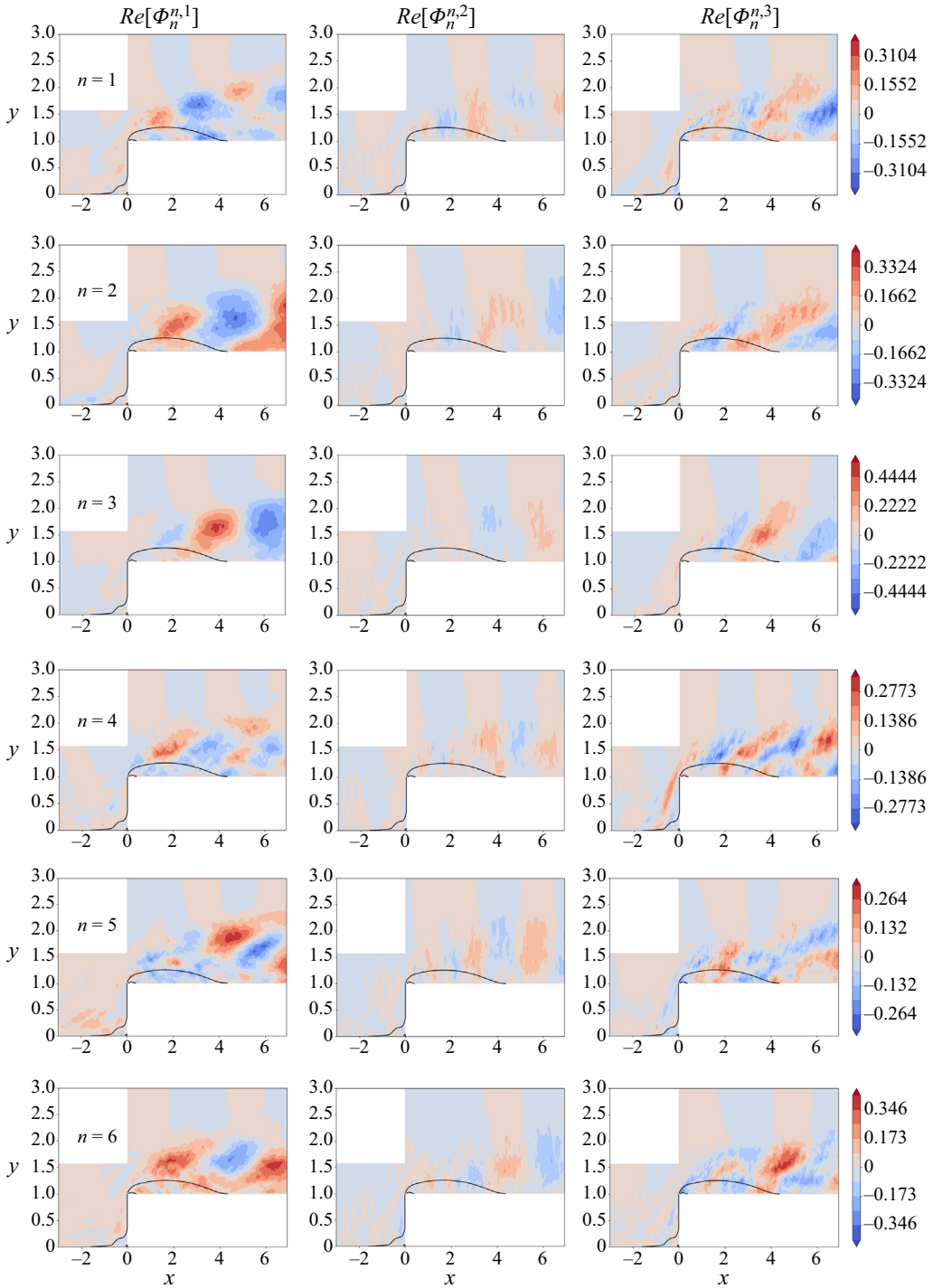


Figure 15. The POD eigenmodes $Re[\Phi_n^1]$. From left to right: streamwise, vertical and spanwise component of the mode. The black line represents the contour $\langle U \rangle = 0$.

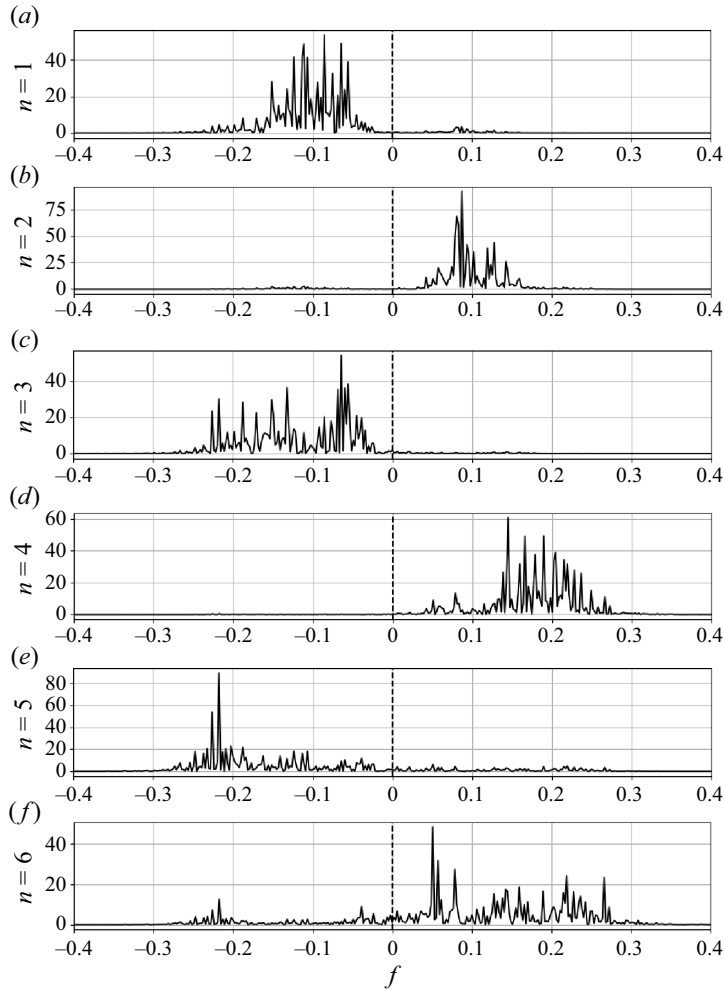


Figure 16. Temporal spectrum of the POD amplitudes $|\hat{a}_1^n|^2$.

5.3. Convection velocity

Comparison of figures 15 and 16 suggests that large scales tend to be associated with low frequencies. However, as shown by Buxton, de Kat & Ganapathisubramani (2013) in the case of a mixing layer, different scales can be associated with different convection velocities. Convection velocities are typically determined from correlation-based methods (Wills 1964). Here, for the mode $k = 1$, we use the spatio-temporal splitting induced by POD to infer a convection velocity C_n for each POD mode n as follows.

- (i) We first extract for each amplitude a_1^n a characteristic frequency f_1^n such that

$$f_1^n = \frac{\int_f |\hat{a}_1^n(f)|^2 f}{\int_f |\hat{a}_1^n(f)|^2}, \quad (5.1)$$

where f spans the space of positive and negative discrete frequencies.

- (ii) We compute the streamwise Fourier components $\hat{\Phi}_k^n(l, y)$ of the spatial mode $\Phi_1^n(x, y)$. It is defined as $\hat{\Phi}_k^n(l, y) = \int_{\Omega_x^{ds}} \Phi_k^n(x, y) \exp(-2i\pi lx/L_{\Omega_x}^{ds}) dx$, where l is the streamwise wavenumber and $\Omega_x^{ds} = [0, L_{\Omega_x}^{ds}]$ is the streamwise domain over which the transform is taken. We then extract a characteristic wavenumber l_m^n from

$$l_1^n = \frac{\sum_l \int_1^{y_f} |\hat{\Phi}_1^n(l, y)|^2 l dy}{\sum_l \int_1^{y_f} |\hat{\Phi}_1^n(l, y)|^2 dy}, \tag{5.2}$$

where l spans the space of streamwise wavenumbers. The streamwise Fourier transform was applied to the downstream region $\Omega_x^{ds} = [0, 7]$ over a vertical region $\Omega_y^{ds} = [1, 7]$. End effects due to the non-periodicity of the domain were not found to affect significantly the value of l_1^n .

- (iii) The convection velocity for each POD mode is then computed as

$$C_1^n = \frac{f_1^n}{l_1^n}. \tag{5.3}$$

The method described above can be adapted to extract a convection velocity for each pair of spanwise invariant modes, by defining complex modes of the form $\underline{\Psi}_0^n = \underline{\Phi}_0^{2n-1} + i\underline{\Phi}_0^{2n}$, associated with complex amplitudes $z_0^n = a_0^{2n-1} - ia_0^{2n}$, so that

$$a_0^{2n-1} \underline{\Phi}_0^{2n-1} + a_0^{2n} \underline{\Phi}_0^{2n} = \text{Re}[z_0^n \underline{\Psi}_0^n]. \tag{5.4}$$

For the n th pair of POD modes (a_0^{2n-1}, a_0^{2n}) , one then defines a characteristic frequency f_0^n as

$$f_0^n = \frac{\sum_f |z_0^n(f)|^2 f}{\sum_f |z_0^n(f)|^2}, \tag{5.5}$$

and a characteristic streamwise wavenumber l_0^n as

$$l_0^n = \frac{\sum_l \int_1^{y_f} |\hat{\Psi}_0^n(l, y)|^2 l dy}{\sum_l \int_1^{y_f} |\hat{\Psi}_0^n(l, y)|^2 dy}. \tag{5.6}$$

The convection velocity for the n th pair is then given by $C_0^n = f_0^n/l_0^n$.

Figure 17 shows the convection velocity for the most energetic POD modes for $k = 0$ (a) and $k = 1$ (b). For almost all modes, the convection velocity is between 0.5 and 0.7, which is in excellent agreement with results from Largeau & Moriniere (2007) (0.5–0.62), Camussi *et al.* (2008) (0.4–0.7), Hoarau *et al.* (2006) (0.7), Kiya & Sasaki (1983) (0.5–0.7). The exception is mode $n = 5$ at $k = 1$, for which the convection velocity is closer to 1, which suggests that the convective motion there is driven by the external flow. This is consistent with the higher frequencies observed in figure 16, as well as the spatial

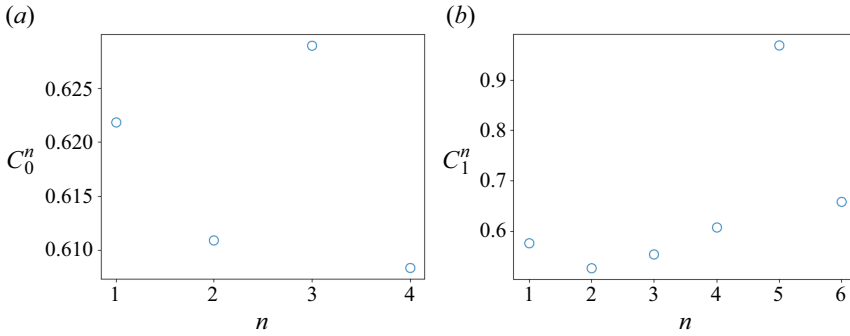


Figure 17. Convection velocity for (a) the pair of POD modes (a_0^{2n-1}, a_0^{2n}) and (b) the modes a_1^n . See text for description.

localization of the mode, which appears to take large values in the external part of the shear layer, further away from the recirculation and from the wall, as evidenced by $\phi_1^{5,1}$ in figure 15.

6. Connection between the recirculation zones

We now determine how the dominant spatio-temporal features of the regions upstream and downstream of the step are related to their respective recirculations. We then examine whether the two recirculations can be connected with each other.

Following Pearson *et al.* (2013), Fang *et al.* (2021), we define reverse flow regions using the indicator

$$I(x, y, z, t) = 1 \quad \text{if } u(x, y, z, t) < 0 \quad \text{and} \quad I(x, y, z, t) = 0 \quad \text{if } u(x, y, z, t) \geq 0. \quad (6.1)$$

For each spanwise position z and instant t , we define upstream and downstream areas of backflow as

$$A^{up}(z, t) = \int_{x=-6}^{x=0} \int_{y=0}^1 I(x, y, z, t) \, dx \, dy \quad (6.2)$$

and

$$A^{ds}(z, t) = \int_{x=0}^{x=7} \int_{y=1}^7 I(x, y, z, t) \, dx \, dy. \quad (6.3)$$

The limits of the integration domains were chosen large enough to enclose the recirculation zones. The dynamics of the upstream and downstream recirculations can thus be monitored through the spatio-temporal variations of the corresponding backflow regions. The volume of these regions V^{up} and V^{ds} can be obtained by integrating the areas over the spanwise dimension:

$$V^{up}(t) = \int_{z=0}^{\pi} A^{up}(z, t) \, dz \quad (6.4)$$

and

$$V^{ds}(t) = \int_{z=0}^{\pi} A^{ds}(z, t) \, dz. \quad (6.5)$$

The time evolution of the backflow volumes V^{up} and V^{ds} is represented in figure 18(a). The maximum cross-correlation between the upstream and downstream volumes, shown

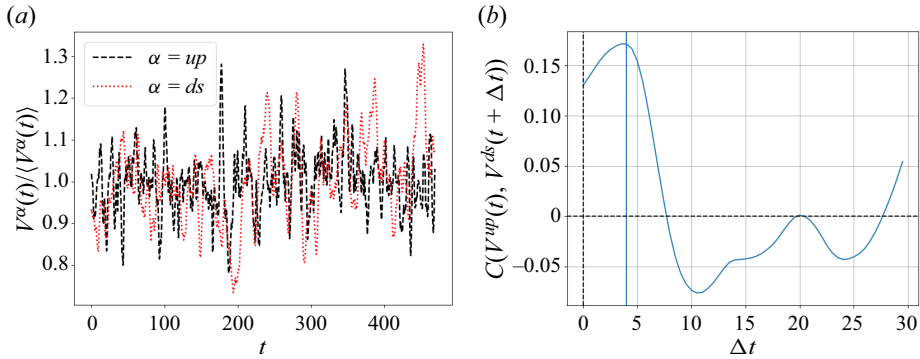


Figure 18. (a) Time evolution of the backflow volumes V^{up} and V^{ds} upstream and downstream of the step. (b) Cross-correlation between V^{up} and V^{ds} .

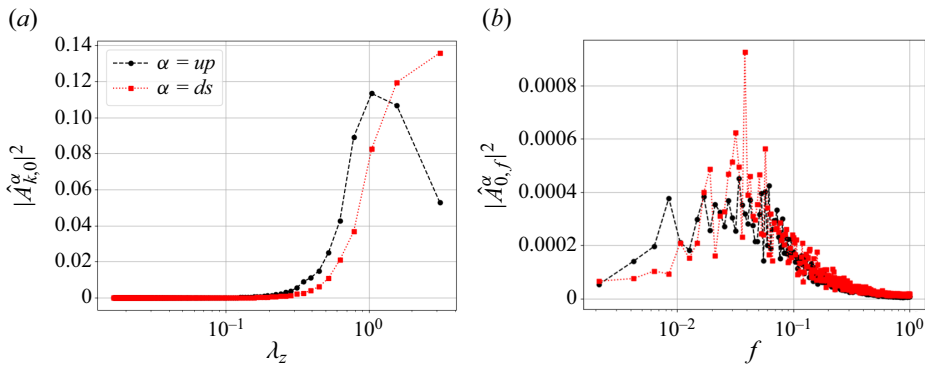


Figure 19. (a) Spatial spectra of the upstream and downstream backflow regions $\hat{A}_{k,0}$. (b) Premultiplied frequency spectra of the upstream and downstream areas of the reverse flow $\hat{A}_{0,f}$. The spectra have been normalized by their variance. The upstream and downstream regions respectively correspond to the black dashed and red dotted lines.

in figure 18b), is of the order of 0.15 for a time delay of 4 units, which does not suggest a clear connection. We note that generally due to experimental constraints, discussions of the areas of reverse flow in the literature (Pearson *et al.* 2013; Graziani *et al.* 2018; Fang *et al.* 2021) are generally focused on the 2-D areas A corresponding to the same longitudinal plane.

The spatio-temporal characteristics of the areas of reverse flow A^{up} and A^{ds} are shown in spectral space in figure 19. The dominant wavelengths are found to be respectively about 1 and 3 for the upstream and downstream regions and the dominant frequencies were in the range $[0.01, 0.1]$. This is in good agreement with the results of Fang *et al.* (2021), who computed similar spectra for an embedded step ($\delta/H > 1$) and identified characteristic wavelengths of 1.32 and 2.68 for respectively the upstream and downstream regions. They also found frequencies in the range $[0.03 - 0.1]$ for both recirculations.

6.1. Global dynamics

We first determine how the spatio-temporal modulations of the backflow regions are connected with the dominant POD modes identified in each region. For the upstream region, figure 20 shows the cross-correlation between the time variations of the volume

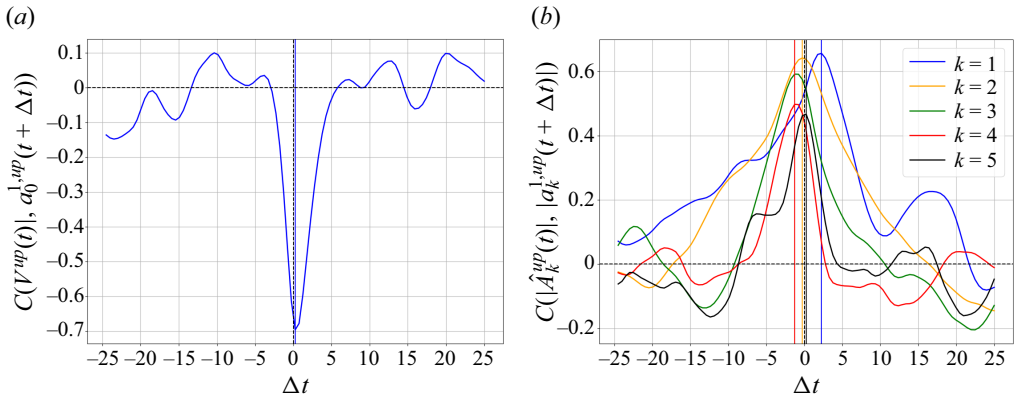


Figure 20. (a) Cross-correlation between the upstream backflow volume V^{up} and the spanwise-averaged velocity amplitude $a_0^{1,up}$. (b) Cross-correlation between the spatial modulations of the upstream area of the reverse flow \hat{A}_k^{up} and the dominant amplitudes of the POD modes in the upstream region $|a_k^{1,up}|^2$.

V^{up} and of the dominant spanwise-averaged fluctuating mode $a_0^{1,up}$. The correlation coefficient between the two curves is -0.7 and is maximal in absolute value for a zero time delay. The negative correlation indicates that the recirculation zone grows when the amplitude of the mode decreases, as discussed in § 4. This high correlation is consistent with the relative importance at a zero spanwise wavenumber of the dominant eigenvalue $\lambda_0^{1,up}$ (see figure 6), and shows that the variations of the backflow volume reflect those of the most energetic 2-D fluctuation.

As was also seen in § 4, a large part of the fluctuation energy is associated with non-zero spanwise wavenumbers. Figure 20 compares for each spanwise wavenumber $k = 1$ to 5, the temporal cross-correlation of the Fourier components of the area of reverse flow $|\hat{A}_k^{up}|$ with those of the dominant fluctuations $|a_k^{1,up}|^2$. The maximum correlation is relatively high (in the range 0.5–0.6) for an optimal time delay that is negative and less than one time unit for $k > 1$. The physical significance of this time delay is not clear, especially as correlation values remain high at zero time delay. The high correlation indicates that the spatial variations of the upstream recirculation are strongly connected with the most energetic fluctuations in the upstream zone, which confirms the relevance of the characteristic structure identified in § 4.

In the downstream region, as more eigenmodes contribute to the motion at the dominant wavenumbers, the influence of the velocity fluctuations was examined using aggregated contributions $q_k = \sum_{n=1}^N E_k^n$, with $E_k^n = \lambda_k^n |a_k^n|^2$ and $N = 10$ (which represents about 50 % of the kinetic energy at this wavenumber). The cross-correlation between these aggregated contributions and the downstream backflow volume V^{ds} is shown in figure 21. No significant correlation was observed for the spanwise invariant modes, which can be expected in view of their low contribution to the fluctuations in the downstream recirculation. In contrast, a significant negative correlation (-0.49) was obtained for the dominant first wavenumber. The maximal anti-correlation reached -0.7 when higher spanwise wavenumbers were included (up to $k = 9$), which confirms the importance of the lowest mode $k = 1$. The optimal time delays were small, i.e. of the order of 1–2 time units, and negative. Although it may be difficult to interpret these time delays, the fact that they are negative is consistent with the idea that the downstream separation zone is

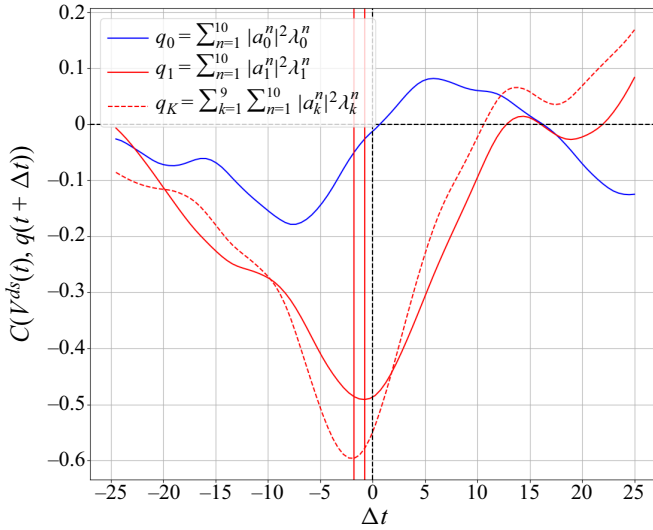


Figure 21. Correlation between the temporal variations of the downstream backflow volume V^{ds} and the amplitudes of the global POD modes.

influenced by the development of the shear layer above it as well as the dominant POD modes at $k = 1$ that characterize it.

We also computed various cross-correlations between the upstream fluctuations and the downstream backflow area (not shown). No correlation larger than 0.25 in absolute value was obtained. This points to a significant reorganization of the flow past the edge of the step, which we attempt to track using local indicators in the next section.

6.2. Local dynamics at the edge

We now discuss the connection between the upstream velocity fluctuations and the downstream recirculation with a focus on the dynamics at the edge of the step. Figure 22 shows, for two different instants t_{min} and t_{max} , a horizontal and a vertical section of the streamwise velocity field respectively located upstream of the step at a height of $y = 0.9$ and directly downstream of the edge at $x = 0.02$ (the sections are represented in figure 23a). The two instants correspond to the times t_{min} and t_{max} for which the downstream backflow volume V^{ds} is respectively minimal and maximal. For both times, the streamwise velocity is organized into a similar streaky pattern that persists from the horizontal to the vertical plane. However, the streaks are more intense when the volume of reverse flow is maximal: the plane-averaged backflow in the horizontal plane at t_{max} is larger by 70 %, and its maximum value is more than twice as high than at t_{min} , while the vertical extent of the most intense streaks in the vertical plane at t_{max} is higher, and can reach above the recirculation height (0.25). This suggests that the downstream separation zone is influenced by the incoming flow and, in particular, the streaks associated with ejections of low-speed fluid at the step edge.

A quantity of interest to characterize instantaneous upstream dynamics is therefore the spanwise-averaged flux of streamwise velocity that crosses the plane $y = 1$ at the edge, a measure of which is given by the momentum deficit

$$-M_e = -\frac{1}{L_z} \int_0^{L_z} [uv](x = -e, y = 1, z) dz \quad \text{where } e = 0.02. \quad (6.6)$$

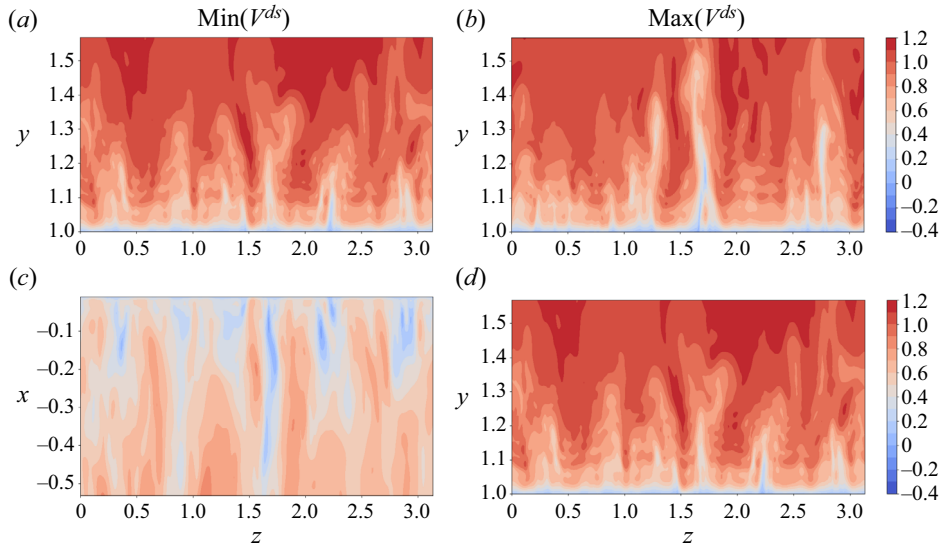


Figure 22. Instantaneous streamwise velocity in the vertical (*a,b*) and horizontal (*c,d*) planes respectively indicated in dark blue and bright green in figure 23. (*a,c*) Time at which the downstream backflow volume V^{ds} is minimum, (*b,d*) time at which the downstream backflow volume V^{ds} is maximum.

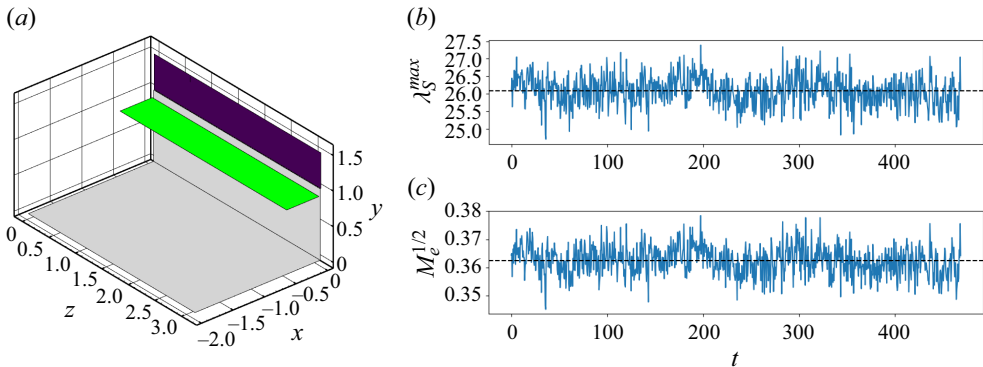


Figure 23. (*a*) Position of the two section planes represented in figure 22 at $y = 0.9$ and $x = 0.01$. (*b*) Top: evolution of the maximum principal stretching eigenvalue λ_s^{max} in the plane $x = 0.01$ (see text for definition). Bottom: evolution of the momentum injected at the edge $M_e^{1/2}$ along the line ($x = -0.02, y = 1$). The dashed lines correspond to the time-averaged values.

A local characteristic time scale τ^{up} for the ejection process can be built from the velocity scale $U_e = M_e^{1/2}$ and a characteristic distance d^{up} , which should be a fraction of the step height and can be tentatively estimated as $d^{up} \approx 0.2 - 0.4$, based on the location of the fluctuation peaks. This yields

$$\tau^{up} = \frac{d^{up}}{M_e^{1/2}} \quad \text{with } d^{up} \approx 0.3. \tag{6.7}$$

Downstream of the step, the development of perturbations in the shear layer should occur on a time scale τ^{ds} that varies like $1/\delta_\omega$, where δ_ω is a characteristic length scale. From Ho & Huerre (1984), the initial maximal spatial growth rate of the shear

layer instability is of the order of $0.12/\delta_S$ where δ_S is the shear layer thickness, so that $\delta_\omega \sim C^{ds}\delta_S$ with $C^{ds} = 1/0.12 \approx 8$. A measure of the shear layer thickness δ_S can be obtained from the inverse of the largest positive eigenvalue λ_S of the mean strain rate $\frac{1}{2}(\nabla\mathbf{U} + \nabla\mathbf{U}^T)$, which was used by Fang *et al.* (2021) to track the position of the shear layer. In a similar fashion, we define an instantaneous shear layer thickness based on the maximal value of the largest positive eigenvalue of the spanwise-averaged strain rate in the vertical plane directly downstream of the edge:

$$\lambda_S^{max}(t) = \max_y \lambda_S(x = 0.01, y, t). \tag{6.8}$$

The time-averaged location of the maximum corresponds to a vertical distance of $y = 0.02$ above the edge. The local time scale at the edge of the shear layer τ^{ds} can therefore be estimated as

$$\tau^{ds} = \frac{1}{\delta_\omega} = \frac{C^{ds}}{\delta_S} \sim \frac{C^{ds}}{\lambda_S^{max}} \quad \text{with } C^{ds} \sim 8. \tag{6.9}$$

Figure 23 compares the time evolution of the characteristic velocity for the ejection process $U_e = M_e^{1/2}$ with the shear layer time scale λ_S^{max} . Both signals are almost perfectly correlated with a correlation coefficient of 0.95. We point out that we computed several other correlation coefficients based on the spanwise-averaged velocity, such as that between the wall shear and M_e , as well as that between λ_S^{max} and the velocity modulus. All coefficients were significantly inferior to the 0.95 value, which means that the match does not simply reflect the fact that the two signals M_e and λ_S^{max} are based on the spanwise-averaged velocity measured at two nearby locations. In addition, both signals have nearly the same root mean square to mean value, which suggests that they are directly proportional to each other, with a ratio $\langle \lambda_S^{max} \rangle / \langle M_e^{1/2} \rangle$ of about 60. This leads to a ratio for τ^{up} / τ^{ds} of about $60d^{up} / C^{ds} \approx 2.25$, which is sufficiently close to 1 for τ^{up} and τ^{ds} to be considered of the same order, given the crudeness of our estimates. This suggests that the shear layer dynamics instantaneously adapt to the upstream ejections, so that a decrease in ejections will immediately trigger a faster development of the shear layer perturbations. A direct connection is therefore established between the momentum deficit associated with the ejections and the strength of the shear layer downstream of the step.

To get a better understanding of this connection, we define an extended correlation coefficient to measure the cross-correlation between the complex Fourier amplitudes of the momentum deficit $-\hat{M}_{e,k}$ and those of the backflow areas \hat{A}_k^α with $\alpha \in \{up, ds\}$. Since M_e is a small-scale, highly intermittent quantity, the signals were time filtered using a moving average of 5 convective time units corresponding to less than one characteristic shedding time. The extended correlation coefficient \bar{C} is defined as

$$\bar{C}(q_1, q_2) = \frac{Re[\langle (\bar{q}_1 - \langle q_1 \rangle)(\bar{q}_2 - \langle q_2 \rangle)^* \rangle]}{|\bar{q}_1|^{rms} |\bar{q}_2|^{rms}}, \tag{6.10}$$

where \bar{q} represents the time-filtered version of q , $\langle q \rangle$ its time average and $|\bar{q}|^{rms}$ the standard deviation of its filtered modulus. Results are presented in figure 24 for the upstream recirculation (a) and the downstream recirculation (b). For Fourier modes $1 \leq k \leq 5$, the correlation between $-\hat{M}_{e,k}$ and the upstream recirculation is strong – larger than 0.6 – with optimal time delays inferior to one time unit (a slightly larger time delay of 3 units is observed for the less energetic mode $k = 1$). This shows that the modulations of the recirculation at the bottom of the step are directly connected with the ejections at the edge, and that both match the variations of the characteristic structure identified in § 4.

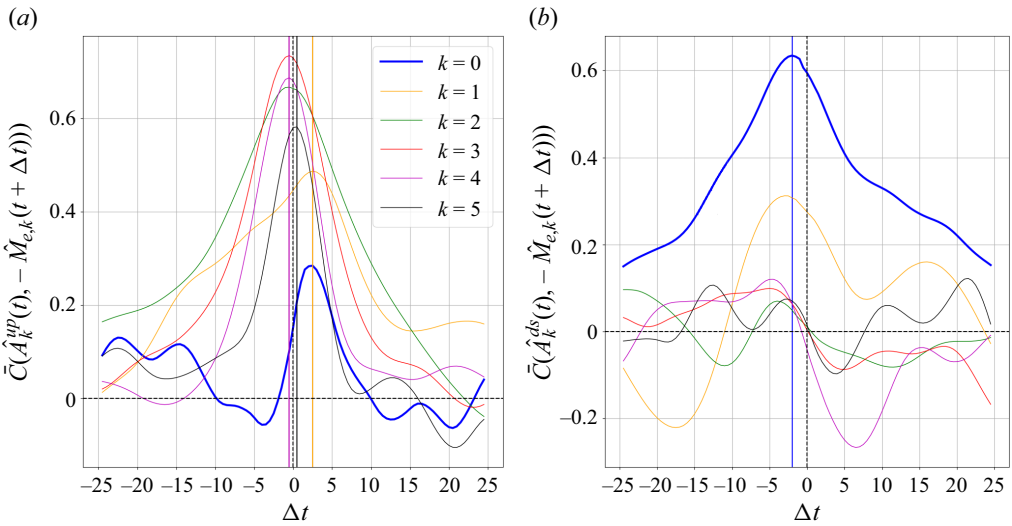


Figure 24. Cross-correlation \bar{C} between the spanwise Fourier components of the upstream (a) and downstream (b) areas of the reverse flow \hat{A}_k and those of the momentum deficit $-\hat{M}_{e,k}$. The signals are filtered with a moving average of 5 time units. See text for a definition of \bar{C} .

It is interesting to contrast these results with those obtained for the downstream recirculation. Only the spanwise-averaged area (or volume) of reverse flow V^{ds} is well correlated – with a correlation coefficient larger than 0.6 – with the average momentum deficit $-\hat{M}_{e,0}$, indicating that an increase in momentum deficit at the edge of the step results in a larger recirculation downstream. The corresponding optimal time delay was positive and of the order of 2 convective time units. Interestingly, no such correlation was detected for higher modes, which confirms a fast reorganization of the flow downstream of the step (and was also substantiated by examination of instantaneous fields).

We therefore propose the following description, summarized in figure 25: low-speed fluid is entrained into the upstream recirculation bubble and ejected with a strong spanwise motion into low-velocity streaks over the edge of the step. The global momentum deficit due to these local ejections impacts the development of the shear layer and the downstream recirculation, although the fluctuations are quickly reorganized. A higher ejection rate (low M_e) leads to a weaker development of the shear layer and a larger recirculation zone. The flow in the shear layer is characterized by a low spanwise modulation, but becomes more two dimensional downstream of the reattachment.

7. A model for the dominant POD velocity amplitudes

7.1. The POD-based models

In this section we propose a model to reconstruct the dynamics of the most energetic POD modes, which are characterized by a range of low frequencies. The model is based on a simplified version of the POD-based models obtained by projection of the Navier–Stokes equations onto the basis of the spatial POD modes. The construction of dynamical systems to predict the amplitudes of the POD modes was first proposed by Aubry *et al.* (1988) and a thorough discussion can be found in Holmes *et al.* (1996).

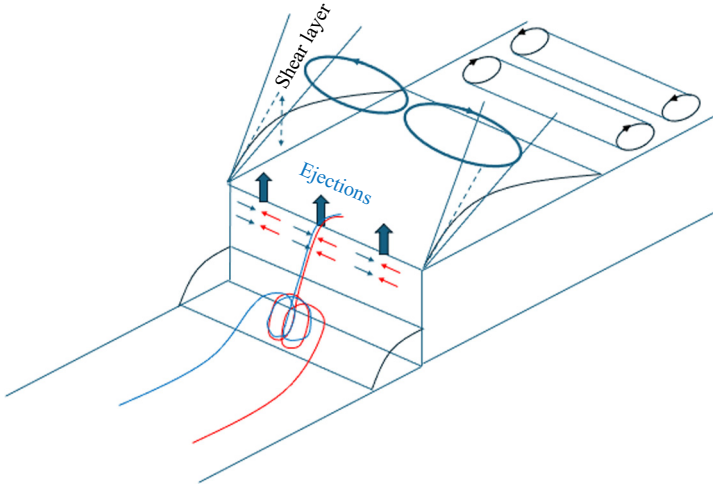


Figure 25. Sketch of the dynamics of the forward-facing step.

Its general form for the set of normalized amplitudes a_k^n with $k \in \{-K, \dots, K\}$ and $n \in \{1, \dots, N_T\}$ can be given as

$$\dot{a}_k^n = A_k^{nm} a_k^m + Q_{kk'}^{nmp} a_k^m a_{k-k'}^p + T_k^n, \quad (7.1)$$

where Einstein notation has been used.

The linear component A_k^{nm} can be further decomposed as

$$A_k^{nm} = D_k^{nm} + L_k^{nm}, \quad (7.2)$$

where D_k^{nm} corresponds to the diffusion term

$$D_k^{nm} = \frac{1}{Re} \sqrt{\frac{\lambda_k^m}{\lambda_k^n}} \iint \phi_k^{n,i*} \left(-k_z^2 + \frac{\partial^2}{\partial x^2} + \frac{\partial^2}{\partial y^2} \right) \phi_k^{m,i} dx dy, \quad (7.3)$$

and L_k^{nm} represents the interaction with the mean mode

$$L_k^{nm} = -\sqrt{\frac{\lambda_k^m}{\lambda_k^n}} \iint \left(\phi_k^{n,i*} U_j \frac{\partial \phi_k^{m,i}}{\partial x_j} + \phi_k^{n,i*} \phi_k^{j,m} \frac{\partial U_i}{\partial x_j} \right) dx dy. \quad (7.4)$$

We denote by $Q_{kk'}^{nmp}$ the interaction coefficient due to the nonlinear term $\underline{q} \cdot \nabla \underline{q}$ in the Navier–Stokes equations ($\underline{q} \cdot \nabla \underline{q}$ represents the velocity fluctuation). It can also include the effect of the pressure gradient if it is not neglected (see Noack, Papas & Monkewitz 2005).

We denote by T_k^n the effect of the modes that are excluded from the truncation

$$T_k^n = \int \hat{\tau}_k^i \phi_k^{m,i*} dx dy - Q_{kk'}^{nmp} a_k^m a_{k-k'}^p, \quad (7.5)$$

where $\hat{\tau}_k^i$ is the Fourier transform of $q_j(\partial q_i / \partial x_j)$.

Here T_k^n is similar to a subgrid-scale stress term that needs to be modelled with additional assumptions in order to close the equations. The most general form is to assume that

$$T_k^n = \alpha_k^n D_k^{nm} a_{km}, \quad (7.6)$$

where α_k^n is a function that is equivalent to a turbulent eddy viscosity ν_t/ν . In early derivations of the model, α_k^n was assumed to be constant (Aubry *et al.* 1988) but in more

recent implementations (see, for instance, Podvin *et al.* 2021), α_k can be a nonlinear function of the resolved modes a_k^n . Following Osth *et al.* (2014), the turbulent eddy viscosity is assumed to scale with the characteristic velocity of the resolved modes $\sqrt{\sum_{m=1}^{N_T} |a_k^m|^2}$, which can be expanded into a sum of a constant term and a quadratic term $1/2 \sum_{m=1}^{N_T} (\lambda_k^m + |a_k^m|^2)$ (Podvin & Sargent 2017). The proportionality constant is negative so that the effect of T_k^n is to prevent the unphysical growth of fluctuations in the model.

7.2. Linear model

We derive a linearized version of the model for the most energetic POD modes a_k^n , with $k = 0, 1$ and $n \leq 10$. The linear model is based on the assumption that the driving mechanism for the fluctuations is their direct interaction with the mean flow – through convection and deformation by the mean shear. Some justification for this can be found on the large separation between the intensity of the mean velocity and that of the fluctuations (the largest POD eigenvalue is less than 1 %). We therefore assume that the quadratic interaction terms Q , the effect of which is to redistribute energy among the resolved modes, can be neglected.

A second assumption is that the effect of both molecular (D) and turbulent (T) viscosity is also small and is limited to preventing non-physical unbounded growth of the fluctuations without modifying their characteristic frequencies. Figure 26 (top row) shows the spectrum of the matrix L_0 and L_1 for a truncation of 10 modes. Each eigenvalue μ_k^n has a small positive real part, which is much smaller than its imaginary part $\mu_k^n = \text{Re}[\mu_k^n] + i \text{Im}[\mu_k^n]$ with $\text{Re}[\mu_k^n] \ll |\text{Im}[\mu_k^n]|$ (the fact that the real part is positive is physically consistent with the fact that the fluctuations are extracting energy from the mean flow). Figure 26 (bottom row) shows the values of the matrix D_k for the wavenumber $k = 1$ (a similar behaviour was observed for $k = 0$). We can see that D_1 is essentially diagonal. Its values D_1^{nn} are mostly real and negative, and their relatively small magnitudes increase only slightly with n . Therefore, D_k can be considered roughly proportional to the identity matrix as a first approximation,

$$D_k \approx -\eta_k I, \quad \text{with } 0 < \eta_k \ll 1. \tag{7.7}$$

This means that $L_k + D_k$ can be assumed to diagonalize in the same basis B as L with eigenvalues $\mu_k^n - \eta_k = \text{Re}[\mu_k^n] - \eta_k + i \text{Im}[\mu_k^n]$.

Since the closure for the unresolved stresses T_k is based on the properties of the dissipation matrix D_k (7.6), we can further assume that the additional effect of the unresolved stresses is to merely modify the real part of the eigenvalues, with $|\text{Re}[\mu_k^n] - \eta_k(1 + \text{Sup}_p \alpha_k^p)| \ll \text{Im}[\mu_k^n]$. Equation (7.1) can then be approximated as

$$\dot{a}_k^n = (L_k^{nm} + (1 + \alpha_k^n) D_k^{nm}) a_k^m \approx \tilde{L}_k^{nm} a_k^m, \tag{7.8}$$

where \tilde{L}_k diagonalizes in the same basis B as L_k with purely imaginary eigenvalues $i \text{Im}[\mu_k^n]$:

$$\tilde{L}_k = B \begin{bmatrix} i \text{Im}[\mu_k^1] & 0 & \dots \\ 0 & i \text{Im}[\mu_k^2] & \dots \\ \dots & \dots & i \text{Im}[\mu_k^{N_T}] \end{bmatrix} B^{-1}. \tag{7.9}$$

The n th column of the matrix B contains the eigenvector b_k^n associated with the eigenvalue $i \text{Im}[\mu_k^n]$ and expressed in the basis a_k^n . Conversely, each POD amplitude a_k^n can be

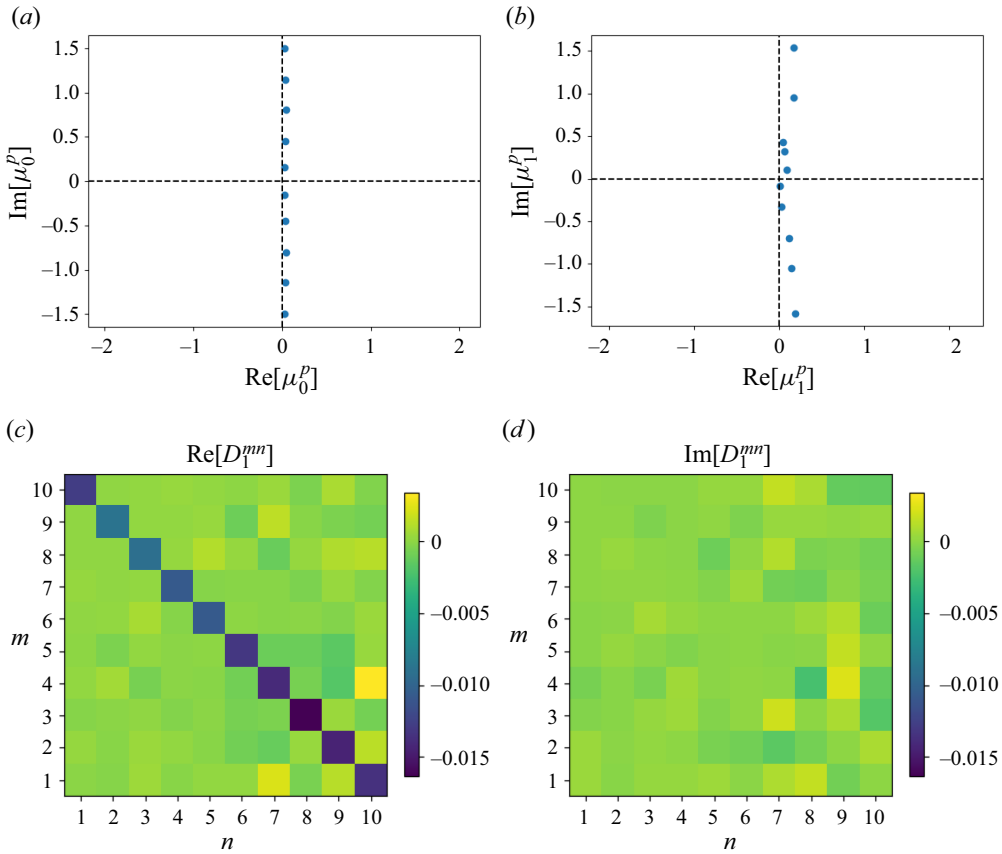


Figure 26. (a,b) Eigenvalues of L_k for a ten-mode truncation for $k = 0$ (a) and $k = 1$ (b). (c,d) Dissipation matrix D_1 real part (c) and imaginary part (d).

represented as a sum of eigenmodes b_k^p : $a_k^n = \sum_{p=1}^{N_T} \beta_k^{np} b_k^p$. Predicted amplitudes for the model can then be reconstructed using

$$a_k^{n,pred}(t) = \beta_k^{np} e^{i \text{Im}[\mu_k^p] t}. \quad (7.10)$$

Figure 27 compares the spectra of the POD amplitudes extracted from the DNS with the frequencies obtained by considering $N_T = 10$ and $N_T = 6$ systems for $k = 0$ and $k = 1$. The predicted spectra shown for each mode n are arbitrarily rescaled by $\text{Max}_p \beta_{np} / \text{Max}_f |\hat{a}_k^n(f)|$ for comparison purposes. We see that in all cases, the prediction provides a good identification of the dominant frequencies of the amplitude spectra, which supports the assumption of the fundamentally linear nature of the dynamics. We emphasize that the model frequencies are solely determined from the spatial modes extracted from the sampled autocorrelation tensor, independently of the sampling rate used to compute the tensor.

7.3. Time-varying linear model

Unlike those of the DNS, the spectra shown in figure 27 are discrete and limited to N_T frequencies, since the linear model has constant coefficients. To make the model more physical, we modify the model so that the strength of the mean mode is allowed to vary in

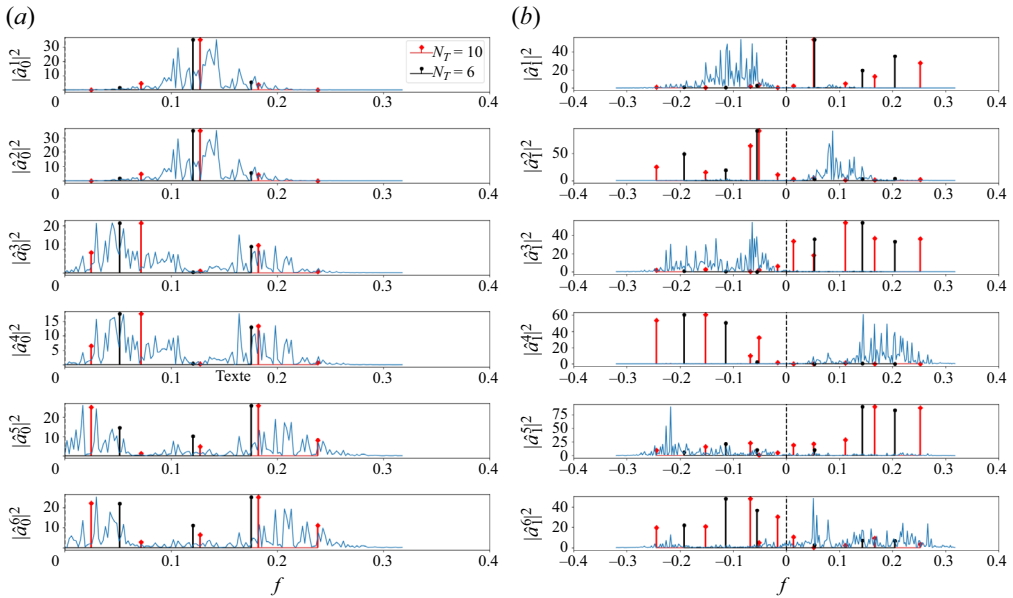


Figure 27. Predicted frequencies of the dominant POD amplitudes with the linear autonomous model (LM) for two different truncations $N_T = 6$ (black lines) and $N_T = 10$ (red lines): (a) $|\hat{a}_0^n|^2$ for $n \in \{1, \dots, 6\}$ and (b) $|\hat{a}_1^n|^2$ $n \in \{1, \dots, 6\}$.

time. As a first approximation, we assume that this variation is solely driven by the local time fluctuations of the mean shear at the edge, which is determined by the maximum stretching eigenvalue λ_S^{max} and, therefore, the ejections over the edge (as evidenced in figure 23). The modified model will be called the forced model.

If ϵ is the time-dependent modulation of the shear layer $\epsilon = \lambda_S^{max} / \langle \lambda_S^{max} \rangle - 1$, the forced model is defined as

$$\dot{a}_k^n = \tilde{L}_k^{nm} (1 + \epsilon) a_k^m. \quad (7.11)$$

For all wavenumbers, the model was integrated from the initial condition $a_k^n = 1$. Using arbitrary initial phases between the modes did not affect the general characteristics reported below. Figures 28(a) and 28(b) show the spectra of the forced model for the modes $k = 0$ and $k = 1$, which can be respectively compared with figures 14 and 16. Although complete agreement should not be expected given the crudeness of our assumption, it can be seen that the model roughly reproduces the widths and heights of the spectral bands of a_k^n observed in the DNS. Figures 28(c) and 28(d) compare the probability distribution functions of the amplitude moduli $|a_k^n|$ for $k = 0$ and $k = 1$ in the DNS, the linear and the forced models. Although some discrepancies are occasionally observed in the distribution tails, both models capture equally well the shape of the distributions, which are characterized by frequent low values for the spanwise invariant modes and a non-zero maximum around 0.5–1 for the spanwise modes.

8. Conclusion

The dynamics of the flow over a forward-facing step have been investigated in a 3-D POD framework using a Fourier representation in the spanwise direction. An energy-rich characteristic structure was extracted from the fluctuations in the upstream region.

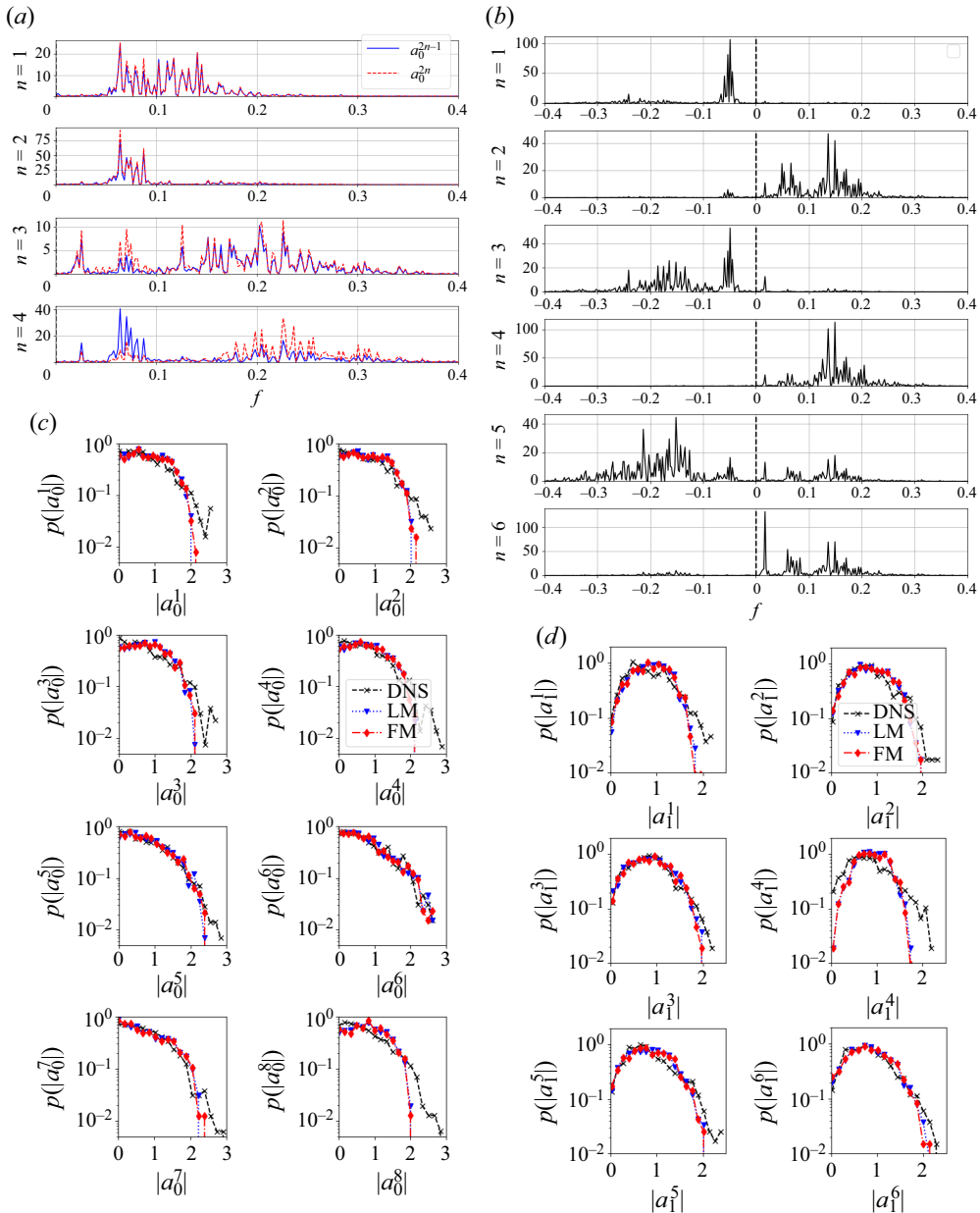


Figure 28. (a) Predicted spectrum of the dominant POD amplitudes $|\hat{a}_0^n|^2$ with the forced model (FM). (b) Predicted spectrum of the dominant POD amplitudes $|\hat{a}_1^n|^2$. (c) Histograms of the amplitude moduli $|a_0^n|$, $n \in \{1, 8\}$ for the DNS, linear model (LM) and FM. (d) Histograms of the amplitude moduli $|a_1^n|$, $n \in \{1, 6\}$ for the DNS, LM and FM.

The spanwise size of the structure scales with the step height H and its formation appears to be associated with a centrifugal instability, the origin of which is located close to the edge of the step. Through the flow modulation created by the structure, incoming fluid close to the bottom wall can get trapped in or around the upstream recirculation then be

ejected over the step into longitudinal packets, along with low-speed fluid collected along the step face through strong spanwise motions.

The following scenario connecting the dynamics of the upstream and the downstream recirculations is proposed: the strong ejections associated with the upstream flow deformation create an instantaneous momentum deficit at the edge of the step, which directly modifies the maximal shear rate in the downstream shear layer, thus impacting its development and the size of the downstream recirculation. A higher volume of ejections reduces the shear rate and increases the downstream recirculation. The flow immediately behind the step is dominated by a spanwise modulation of characteristic wavelength $\lambda_z = \pi H$, while spanwise rolls are observed downstream of reattachment. Since the wavelength λ_z corresponds to the span of the periodic domain, more investigations would be needed to establish whether this result can be generalized to wider domains. Both 3-D fluctuations in the shear layer and 2-D motions behind the recirculation are characterized by convection velocities of about $0.6 U$, where U is the incoming velocity.

A linear model based on the direct interaction of the mean flow with the POD spatial modes at these dominant wavenumbers was able to predict the characteristic frequencies of the mode amplitudes. The modulations in the frequency spectra appear to be consistent with the variations of the instantaneous maximal shear rate at the edge of the step, and therefore, with those of the ejections. This suggests that linear mechanisms play a key role in the global flow dynamics and that these dynamics could be monitored through local indicators at the step edge, which opens up interesting possibilities for control. However, more investigations are needed to confirm this potential. In particular, linear stability analysis as well as resolvent-based approaches would be helpful to better understand the formation and characteristics of the upstream structure.

Acknowledgements. The DNS results used in this study are part of the database <https://datasetmeca.lisn.upsaclay.fr/>. We are grateful to E. Larose, R. Martinuzzi and F. Kerhervé for several helpful discussions. We express our thanks to the anonymous referees for their insightful suggestions.

Funding. This work was performed using HPC resources from GENCI-IDRIS (grant 2023-AD012A020 62R2).

Declaration of interest. The authors report no conflict of interest.

Author ORCID.

 B. Podvin <https://orcid.org/0000-0001-7003-719X>.

REFERENCES

- AUBRY, N., HOLMES, P., LUMLEY, J.L. & STONE, E. 1988 The dynamics of coherent structures in the wall region of the wall boundary layer. *J. Fluid Mech.* **192**, 115–173.
- BEAM, R.M. & WARMING, R.F. 1976 An implicit finite-difference algorithm for hyperbolic conservation-law form. *J. Comput. Phys.* **22**, 87–110.
- BEAUDOIN, J.-F., CADOT, O., AIDER, J.-L. & WESFREID, J.E. 2004 Three-dimensional stationary flow over a backward-facing step. *Eur. J. Mech. (B/Fluids)* **23** (1), 147–155.
- BRÈS, G.A. & COLONIUS, T. 2008 Three-dimensional instabilities in compressible flow over open cavities. *J. Fluid Mech.* **599**, 309–339.
- BUXTON, O.R.H., DE KAT, R. & GANAPATHISUBRAMANI, B. 2013 The convection of large and intermediate scale fluctuations in a turbulent mixing layer. *Phys. Fluids* **25** (12), 125105.
- CAMUSSI, R., FELLI, M., PEREIRA, F., ALOISIO, G. & MARCO, A.D. 2008 Statistical properties of wall pressure fluctuations over a forward-facing step. *Phys. Fluids* **20** (7), 075113.
- DAGAUT, J., NEGRETTI, M.E., BALARAC, G. & BRUN, C. 2021 Linear to turbulent Görtler instability transition. *Phys. Fluids* **33** (1), 014102.
- DRAZIN, P.G. & REID, W.H. 1982 *Hydrodynamic Stability*. Cambridge University Press.

- ERM, L.P. & JOUBERT, P.N. 1991 Low-Reynolds-number turbulent boundary layers. *J. Fluid Mech.* **230**, 1–44.
- FANG, X. & TACHIE, M.F. 2020 Spatio-temporal dynamics of flow separation induced by a forward-facing step submerged in a thick turbulent boundary layer. *J. Fluid Mech.* **892**, A40.
- FANG, X., TACHIE, M.F., BERGSTROM, D.J., YANG, Z. & WANG, B.-C. 2021 Three-dimensional structural characteristics of flow separation induced by a forward-facing step in a turbulent channel flow. *J. Fluid Mech.* **919**, A24.
- FARABEE, T.M. & CASARELLA, M.J. 1986 Measurements of fluctuating wall pressure for separated/reattached boundary layer flows. *ASME J. Vib. Acoust. Stress Reliab.* **108** (108), 301–307.
- FAUGARET, A., DUGUET, Y., FRAIGNEAU, Y. & MARTIN-WITKOWSKI, L. 2022 A simple model for arbitrary pollution effects on rotating free-surface flows. *J. Fluid Mech.* **935**, A2.
- FRAIGNEAU, Y. 2024 SUNFLUIDH: a research software for the computational fluid dynamics. User's Guide (last release). Available at: <https://sunfluidh.lisn.upsaclay.fr>. LISN.
- GODA, K. 1979 A multistep technique with implicit difference schemes for calculating two- or three-dimensional cavity flows. *J. Comput. Phys.* **30**, 76–95.
- GRAZIANI, A., KERHERVÉ, F., MARTINUZZI, R.J. & KEIRSBULCK, L. 2018 Dynamics of the recirculating areas of a forward-facing step. *Exp. Fluids* **59**, 154.
- GUERMOND, J.L., MINEV, P.D. & SHEN, J. 2006 An overview of projection methods for incompressible flows. *Comput. Meth. Appl. Mech. Engng* **195**, 6011–6045.
- HAHN, C. 2008 Experimentelle Analyse und Reduktion aeroakustischer Schallquellen an einfachen Modellstrukturen. PhD thesis, Universität Erlangen-Nürnberg.
- HAMMOND, D.A. & REDEKOPP, L.G. 1998 Local and global instability properties of separation bubbles. *Eur. J. Mech. (B/Fluids)* **17** (2), 145–164.
- HARLOW, F.H. & WELCH, J.E. 1965 Numerical calculation of time-dependent viscous incompressible flow of fluid with free surface. *Phys. Fluids* **8**, 2182–2189.
- HATTORI, H. & NAGANO, Y. 2010 Investigation of turbulent boundary layer over forward-facing step via direct numerical simulation. *Intl J. Heat Fluid Flow* **31**, 284–294.
- HO, C.M. & HUERRE, P. 1984 Perturbed free shear layers. *Annu. Rev. Fluid Mech.* **16**, 365–422.
- HOARAU, C., BORÉE, J., LAUMONIER, J. & GERVAIS, Y. 2006 Analysis of the wall pressure trace downstream of a separated region using extended proper orthogonal decomposition. *Phys. Fluids* **18** (5), 055107.
- HOLMES, P., LUMLEY, J.L. & BERKOOZ, G. 1996 *Turbulence, Coherent Structures, Dynamical Systems and Symmetry*. Cambridge University Press.
- KIYA, M. & SASAKI, K. 1983 Structure of a turbulent separation bubble. *J. Fluid Mech.* **137**, 83–113.
- KIYA, M. & SASAKI, K. 1985 Structure of large-scale vortices and unsteady reverse flow in the reattaching zone of a turbulent separation bubble. *J. Fluid Mech.* **154**, 463–491.
- LANZERSTORFER, D. & KUHLMANN, H.C. 2012 Three-dimensional instability of the flow over a forward facing step. *J. Fluid Mech.* **695**, 390–404.
- LARGEAU, J.F. & MORINIERE, V. 2007 Wall pressure fluctuations and topology in separated flows over a forward-facing step. *Exp. Fluids* **42** (1), 21–40.
- LAROSE, E., KERHERVÉ, F., FRAIGNEAU, Y., PODVIN, B., MORTON, C. & MARTINUZZI, R. 2024 Experimental and numerical investigation of oncoming flow conditions on the dynamics of flow over a forward-facing step. In *Proceedings of the Thirteenth International Symposium on Turbulence and Shear Flow Phenomena (TSFP13)*, 25–28 June, Montréal, Canada.
- LUMLEY, J.L. 1967 The structure of inhomogeneous turbulent flows. In *Atmospheric Turbulence and Radio Wave Propagation* (ed. A.M. Iaglom & V.I. Tatarski), pp. 221–227. Nauka.
- MARINO, L. & LUCHINI, P. 2009 A joint analysis of the flow over a forward-facing step. *Theor. Comput. Fluid Dyn.* **23**, 37–54.
- MARTINUZZI, R.J. & TROPEA, C. 1993 The flow around surface-mounted, prismatic obstacles placed in a fully developed channel flow. *Trans. ASME J. Fluids Engng* **115**, 85–92.
- MCGUINNESS, M. 1978 Flow with a separation bubble—steady and unsteady aspects. PhD thesis, Cambridge University.
- MOIN, P. & MOSER, R. 1989 Characteristic-eddy decomposition of turbulence in a channel. *J. Fluid Mech.* **200**, 471–509.
- MOSS, W.D. & BAKER, S. 1980 Re-circulating flows associated with two-dimensional steps. *Aeronaut. Q.* **31** (3), 151–172.
- NOACK, B., PAPAS, P. & MONKEWITZ, P. 2005 The need for a pressure-term representation in empirical Galerkin models of incompressible shear flows. *J. Fluid Mech.* **523**, 339–365.

- OSTH, J., NOACK, B., KRAJNOCI, S., BORÉE, D. & BARROS, J. 2014 On the need for a nonlinear subscale turbulence term in POD models as exemplified for a high-Reynolds-number flow over an Ahmed body. *J. Fluid Mech.* **474**, 518–544.
- PAMIES, M., WEISS, P.E., GARNIER, E., DECK, S. & SAGAUT, P. 2009 Generation of synthetic turbulent inflow data for large-eddy simulation of spatially evolving wall-bounded flows. *Phys. Fluids* **21**, 045103.
- PEACEMAN, D.W. & RACHFORD, H.H. 1955 The numerical solution of parabolic and elliptic differential equations. *Intl J. Ind. Maths* **3**, 28–41.
- PEARSON, D.S., GOULART, P.J. & GANAPATHISUBRAMANI, B. 2013 Turbulent separation upstream of a forward facing step. *J. Fluid Mech.* **724**, 284–304.
- PODVIN, B., PELLERIN, S., FRAIGNEAU, Y., BONNAVION, G. & CADOT, O. 2021 Low-order modelling of the wake dynamics of an Ahmed body. *J. Fluid Mech.* **927**, R6.
- PODVIN, B. & SERGENT, A. 2017 Precursor for wind reversal in a square Rayleigh–Bénard cell. *Phys. Rev. E* **05** (1), 013112.
- SARIC, W.S. 1994 Görtler vortices. *Annu. Rev. Fluid Mech.* **26** (1), 379–409.
- SHERRY, M., JACONO, D.L. & SHERIDAN, J. 2010 An experimental investigation of the recirculation zone formed downstream of a forward facing step. *J. Wind Engng Ind. Aerodyn.* **98**, 888–894.
- SIPP, D. & JACQUIN, L. 2000 A criterion of centrifugal instabilities in rotating systems. In *Vortex Structure and Dynamics*. Springer.
- SIROVICH, L. 1987 Turbulence and the dynamics of coherent structures. Part I: coherent structures. *Q. Appl. Maths* **45** (3), 561–571.
- SPALART, P.R. 1988 Direct numerical simulation of a turbulent boundary layer up to $Re_\theta = 1410$. *J. Fluid Mech.* **187**, 61–98.
- STUER, H. 1999 Investigation of separation over a forward-facing step. PhD thesis, ETH Zurich.
- STUER, H., GYR, A. & KINZELBACH, W. 1999 Laminar separation on a forward facing step. *Eur. J. Mech. (B/FLuids)* **18** (4), 675–692.
- TANI, I. 1962 Production of longitudinal vortices in the boundary layer along a concave wall. *J. Geophys. Res.* **67**, 3075–80.
- TENAUD, C., PODVIN, B., FRAIGNEAU, Y. & DARU, V. 2016 On wall pressure fluctuations and their coupling with vortex dynamics in a separated-reattached turbulent flow over a blunt flat plate. *Intl J. Heat Fluid Flow* **61**, 730–748.
- WEISS, J., MOHAMMED-TAIFOUR, A. & SCHWAAB, Q. 2015 Unsteady behavior of a pressure-induced turbulent separation bubble. *AIAA J.* **53** (9), 2634–2645.
- WILHELM, D., HARTEL, C. & KLEISER, L. 2003 Computational analysis of the two-dimensional–three-dimensional transition in forward facing step flow. *J. Fluid Mech.* **489**, 1–27.
- WILLS, J.A.B. 1964 On convection velocities in turbulent shear flows. *J. Fluid Mech.* **20** (3), 417–432.